CALIBRATING AND MEASURING BED LOAD TRANSPORT WITH A MAGNETIC DETECTION SYSTEM

by
JASON REMPEL

B.Sc., The University of British Columbia, 2002

A THESIS SUBMITTED IN PARTIAL FULFILLMENT OF THE REQUIREMENTS FOR THE DEGREE
OF

MASTER OF SCIENCE

in

THE FACULTY OF GRADUATE STUDIES
(Geography)

THE UNIVERSITY OF BRITISH COLUMBIA
June 2005

Abstract

A series of lab and flume experiments were designed to test and calibrate the Bed load Movement Detector (BMD), a magnetic system for measuring bed load movement in gravel bed streams. Experiments used both artificial and natural stones, and were specifically designed to isolate the effects of particle size, velocity and magnetic content on the shape of the recorded signal.

Empirical relations were derived between the amplitude, width and integral of the sensor response, with particle size, velocity and magnetic content. Because of high variability in response across an individual sensor, the current system cannot be used to reliably predict the particle size from an individual signal. Results improved at the event scale, where variability averages out. Over the course of the experiments, a number of weaknesses in the sensor design were observed; these are discussed, and some suggestions are made of ways to improve the system.

Table of Contents

List of Tables

List of Figures

Acknowledgements

This thesis is a culmination of two great years of research and learning. It was accomplished with the support of many friends, family and colleagues along the way.

First I would like to thank my supervisor Dr. Marwan Hassan for giving me the opportunity to work with him and to learn from him. I especially appreciate the fact that your door was always open, and that you dropped whatever you were working on to give me your attention when I came knocking.

Second I would like to thank Dr. Randy Enkin from the GSC's Pacific Geoscience Centre. Not only did you give me access to your lab, you spent many hours working through my results with me, helping me to understand them better. I love your enthusiasm.

Thanks to Dr. Dan Moore for many helpful comments that improved the final product; to Jon Tunnicliffe for many discussions, and for teaching me how to use the system; and to Andre Zimmermann for helping me learn how to build the models.

My time at UBC would not have been complete with out the opportunity to work with many others in the department, especially Michael Church, Brett Eaton, Francesco Brardinoni, Dave Campbell, Josh Caulkins and Bonnie Smith.

To my family, and especially to my wife Leah, thanks for your ongoing love and encouragement.

Chapter 1: Introduction

1.1 Research Context:

The entrainment and deposition of sediment from the streambed produces the geometry, or morphology, of a stream channel. The most common morphologies in the Pacific Northwest are the riffle-pool, and step-pool systems (Montgomery and Buffington, 1997). These morphologies help stabilize the channel, and produce the different environments needed for aquatic habitats. Sediment transport and channel morphology are mutually linked and, therefore, changes in the sediment transport regime will be reflected by changes in channel morphology (e.g. Ashmore and Church, 1998). Sediment transport regime may change due to natural events, such as an extreme flood event, the release of sediment from the break up of a log jam, or sediment input from landslide and debris flow activity. It may also be affected by anthropogenic activities such as logging, damming, or gravel mining. Therefore, understanding the processes involved in sediment transport has important implications for management of stream systems.

However, a reliable method for measuring sediment transport, especially bed load is one of the main problems that limits progress in river mechanics research. Sediment transport is a function of the sedimentological character of the bed, the turbulent nature of flow, and the supply of sediment to the stream. These are all independently complex processes that together produce high variability of sediment transport, both spatially and temporally (Reid and Frostick, 1987).

It is generally accepted that discharge is the only independent factor controlling the amount of sediment transport. However, at a constant discharge, the sediment transport rate is highly variable in both time and space (e.g. Hayward and Sutherland, 1974; Reid and Frostick, 1987; Bunte, 1996). This variability raises a number of questions when considering bed load transport. What is the threshold for the entrainment of particles? What sedimentological factors affect the timing and amount of transport? How much sediment is moving? Where is the sediment moving to/from?

1.2 Entrainment Thresholds:

An individual particle will begin moving when the hydraulic forces acting upon it overcome those keeping it in the bed – namely gravity and friction. Hydraulic forces have generally been described in terms of shear stress ($\tau_o = \rho_w gdS$) or stream power ($\Omega = QS\rho_w$) where ρ_w is the density of water [M/L^3], g is gravity [L/T^2], d is water depth [L], S is slope [1] and Q is discharge [L^3/T].

Theoretically, the critical shear stress that will begin entrainment of a particle is proportional to particle size (Shields, 1936). The original experiments by Shields (1936) were run under the simplified case of uniform grain size. Many researchers (e.g. Andrews, 1983; Ashworth and Ferguson, 1989) have extended this theory to natural gravel-bed rivers. Their field evidence supports the idea of "size selective transport", where a given flow has the capacity to move everything less than or equal to a given size fraction.

Parker et al. (1982) and Parker and Klingeman (1982) suggested that in gravel bed streams, where the sediments are widely graded, particle interactions would interfere with movement, making Shield's critical shear stress irrelevant. Instead, they proposed an alternate theory of entrainment where the effect of armouring produces a situation in which all the particles – regardless of size – start moving at once, or are "equally mobile." A coarse-grained armour layer shelters the smaller particles from the hydraulic forces, keeping them in the bed until the hydraulic forces are great enough to cause the larger particles to begin moving. Break up of the armour layer exposes the previously hidden particles, and subsurface material to the flow.

Other particle interactions have also been observed that further enhance armouring processes, including: imbrication (Powell and Ashworth, 1995), pebble clusters (Brayshaw, 1985; Reid and Frostick, 1987), and stone cells (Church et al., 1998). These processes increase the stability of the bed and therefore the critical shear stress required to initiate transport. Church et al. (1998) were able to show that stone cells increase the critical shear stress needed to entrain particles 2-4 times, reducing sediment transport up to 10^3 times.

1.3 Phases of Transport:

Based on both field research and flume experiments, size selective transport, and equal mobility have been identified as different phases of transport that occur as discharge increases. Jackson and Beschta (1982) developed a 2-phase model to describe the transition between types of transport; the model was then extended to a 3-phase model by Ashworth and Ferguson (1989) and Wilcock and McArdell (1993). Phase 1 is "over-passing sand", where fine grains pass over a static bed. In this phase, transport rates are extremely low. As discharge increases, individual particles move from exposed areas in the surface layer as "partial transport" (Phase 2). Phase 3, a "fully mobile" phase, occurs at even higher flows. The largest particles begin to move, allowing the previously sheltered finer particles, and sub-surface material to be exposed to the flow.

Phase 3 transport only occurs under rare flows. Andrews (1994) determined that at Sagehen Creek, 95% of the bed load was transported under partial transport conditions. Data used by Ashworth and Ferguson (1989) to develop their 3-phase model only approached full mobility.

With each phase, the volume and complexity of transport increases; however our ability to measure transport decreases. It is extremely important to be able to measure the highest transport rates, as they are the channel shaping events. Methods of measurement therefore must be capable of accommodating large rates and volumes of transport. A fundamental problem in sediment transport research is that no measurement technique has been commonly accepted as superior, and there are no standard protocols (Hicks and Gomez, 2003).

1.4 Sediment Transport Measurement:

Measuring the amount of sediment transport is difficult, and involves a high level of uncertainty. This is due to a greater than two order of magnitude range of grain size (2 mm to >200 mm) that moves as bed load in gravel-bed rivers, high spatial and temporal variability of movement, large volumes of sediment, and extremely difficult field logistics. A wide range of methods have been employed to measure the amount of sediment transport, the simplest of which are samplers, pit traps, sediment tracers and morphological surveys. A summary of these methods is provided below.

1.4.1 Samplers:

A large number of bed load samplers have been developed, the most common of which is the Helley-Smith Sampler (Helley and Smith, 1971). The instrument can be hand-held or cable mounted. It is placed on the bed of the stream, and has a standard 3" x 3" opening with a net to catch moving sediment. All sampling devices are faced with the same concern: is the sample collected representative of what is actually moving in the bed at the time of measurement?

Any sampler placed on the bed is an obstruction to the flow, which necessarily changes the flow pattern around the sampler. This will change the entrainment conditions and bias sampling, both in terms of the texture and the amount of sediment collected. The exact effect of this is unknown, due to inherent difficulties in calibrating such an instrument (Hubbell, 1987).

Collection of samples is very labour intensive. Sediment is collected via cross-sectional traverses, taking samples at equal increments across the channel width. The number of samples collected, and the length of collection time is dependent on the stream width and the strength of the flow. In order to account for the spatial and temporal variability of transport, multiple traverses should be made (Ryan and Troendle, 1997). Sample duration is generally 30 or 60 seconds (Ryan and Troendle, 1997), however Andrews (1994) took 4-minute samples to better account for random fluctuations and temporal variability. Even with a long sampling duration, the sample still may not be representative; because of the sporadic nature of the movement of large particles, the probability of catching these particles is very low. Also, due to the small opening of the device (3" x 3"), large particles are systematically under represented. Samplers with larger openings have been used, but they are clumsier, and more difficult to work with, especially in strong flows (Ryan and Troendle, 1997).

Due to the irregular shape of the bed surface, the sampler may not sit flush with the bed, and allow particles to pass under it. Also, it is difficult to maintain solid contact with the bed during high flows. In this case, sediment may be missed, or the bed could be disturbed and sediment may be scooped into the sampler (Ryan and Troendle, 1997). In snowmelt dominated catchments, due to diurnal variation, the peak flows are often around midnight (Bunte, 1996; Tunnicliffe, 2000), making measurement even more difficult, or impossible.

1.4.2 Pit Traps:

An alternative to sampling is to install pit traps into the stream. Pit traps may be in the form of buckets (Powell and Ashworth, 1995; Hassan and Church, 2001; Church and Hassan, 2002), or a trough that spans the entire channel width. They are installed in the bed, flush with the bed surface so that they do not disrupt flow. The traps collect all the bed load that moves over them, eliminating the problem of representative sampling. However, they only provide an event scale volume of sediment transport; they give no indication of the temporal variability of transport. During large events, the traps may overfill, in which case data are lost. Installation and maintenance of pit traps may be extremely difficult in the deepest parts of perennial streams, where much of the transport may be occurring.

1.4.3 Indirect Measurement:

Two methods of indirectly determining sediment transport have been developed, one using tracer particles, and the other looking at changes in channel morphology.

Particle tracers have been used to track the 3-dimensional movement of individual particles (Hassan and Ergenzinger, 2003). Particles are selected from the stream, and typically tagged with paint, or inserted magnets; radioactive stones, exotic lithologies and radio transmitters have also been used. The initial location of particles is mapped, and after an event, these particles are recovered. The distance of transport, and depth of burial is recorded. An indirect measure of sediment transport can be estimated, and the depth of the active layer determined. Zones of erosion and deposition can be inferred from the mapping. Recovering the particles is extremely labour intensive, and often the percentage recovered is low, therefore a large sample size is necessary.

The morphological method is based on the direct relationship between sediment transport and changes in channel morphology. Channel morphology is monitored through digital elevation models (DEMs) of the stream built from repeated, high density, cross sectional surveys, high-resolution (4 points/m^2) reach surveys, or photogrammetric methods (Ashmore and Church, 1998). The net volume change can be determined by subtracting DEM surfaces from before and after an event, providing an estimate of the volume of sediment transport. This method is useful for active streams with high instability. Its use is limited in stable streams, where the changes are likely within the error of the method.

The morphological method provides a minimum estimate of annual sediment transport, as multiple cycles of erosion and deposition may have occurred between surveys. The method does highlight regions of scour and deposition, and distance of transport may be inferred (Ashmore and Church, 1998), but like the pit traps and tracers, it provides no resolution of temporal variability.

1.5 Continuous Bed load Measurement Methods:

In order to address the lack of resolution and the problems of representative sampling, a number of methods have been developed to continuously monitor bed load movement. Continuous measurement provides a picture of the temporal variation in transport; some instrument designs can also account for spatial variability across the channel. A number of methods have been developed including the vortex tube sediment trap, the conveyor belt trap, the recording pit trap, acoustic methods, and the magnetic method.

1.5.1 Vortex Tube Sediment Trap:

Adapting an idea used to eject unwanted sand and silt from irrigation canals, a vortex trap is installed in the creek to eject transported sediment to a processing station at the side of the stream. After processing, sediment is reintroduced to the stream downstream of the trap. The trap is oriented at a 45° angle to the flow, creating the vortex that forces the sediment out the side of the trap. Emptying the trap and weighing the sediment at regular intervals allows rates of transport to be calculated.

Vortex systems were used by: Milhous (1973) at Oak Creek, Oregon, Hayward and Sutherland (1974) at Torlesse Stream, New Zealand, O'Leary and Beschta, (1981) at Flynn Creek, Oregon, and Billi and Tacconi (1987) at Virginio Creek, Italy. Hayward and Sutherland (1974) weighed samples every 10 to 20 minutes, while Billi and Tacconi (1987) were able to weigh samples every minute. Peak flows in nival streams may last a number of days, so continuous measurement is a very labour intensive procedure that requires 2-3 workers at any one time. At Torlesse Stream, workers were able to trap, weigh and return all of the sediment to the stream for transport rates up to 2000 kg/hr (Hayward and Sutherland, 1974). At higher transport rates the workers were overwhelmed and a sampling program had to be instituted. At Virginio Creek, a rotating sieve was used to eliminate water and fines. The system was able to process up to 42000 kg/hr (Billi and Tacconi, 1987).

Installation of a vortex system involves building a concrete flume in the creek that houses the trap. The system uses conveyor belts to move material to the weighing station, and to return sediment to the stream. This limits the streams that are suitable for a vortex system to ones with easy access and reliable power supply.

Once the vortex system is installed, the data that it produces are extremely valuable. The trap is capable of efficiently trapping sediment from coarse sands to particles greater that 400 mm in diameter (Hayward and Sutherland, 1974). Limitations to the system are that there is no ability to resolve spatial variability and that at high flows the trapping efficiency may decrease, allowing the sands to over pass the trap (Hayward and Sutherland, 1974).

Leopold and Emmett (1976, 1977) used a similar system on the East Fork River, Wyoming. Sediment was weighed in the same manner as the vortex trap system, but instead of creating a vortex to force sediment out of the trap, a conveyor belt was installed in the bottom of the trap. The system was capable of handling transport rates up to 9000 kg/hr. A spatial component was incorporated by a gate system, which allowed sections of the trap to be analyzed separately (Leopold and Emmett, 1976).

1.5.2 The Recording Trap:

The Birkbeck bed load sampler is a recording pit trap system that was developed by Reid et al. (1980) at Turkey Brook, UK. The installation of this system is much simpler than the vortex and conveyor belt systems. Pit traps were installed with pressure sensitive pillows beneath them. As the traps fill, the increase in pressure is recorded. With a synchronous record of water depth to account for the weight of water, the increase in pressure can be related to the weight of sediment that is filling the trap. Temporal variation in sediment transport can then be seen through the rate of weight increase.

The weight increase is measured electronically, allowing this device to measure sediment transport unmanned. This provides a distinct advantage over the vortex and conveyor belt systems, especially since flows often occur overnight. After the flow subsides, workers empty the traps, and can sieve the collected material to determine a grain size distribution for the transported material. At Turkey Brook, 2 cross-sections with 3 traps each added the ability to resolve spatial variability in transport.

A disadvantage to the recording trap system is that only one grain size distribution can be collected for each event. With the vortex and conveyor belt systems, operators are capable of collecting samples to analyze the change in grain size distribution over an event. Also, during large events, the traps often overfill, thereby missing important data. Overfilling traps is a significant limitation, and therefore, the system is more appropriate for streams with low sediment transport rates.

1.5.3 Acoustic Methods:

A number of researchers have used acoustic methods to record sediment transport. Throne et al. (1989) installed a hydrophone in the bed of a tidal channel. The hydrophone measured sediment generated noise (SGN) from the collisions between particles, which they related to sediment transport. The hydrophone was calibrated against sediment transport rates measured with underwater video.

Similarly, Rickenmann (1994) used nine hydrophones installed in the bed of the Erlenbach stream to record the intensity of bed load transport. By relating the number of impulses recorded to the volume of sediment accumulating in a retention basin, he was able to roughly calibrate the system.

Limitations of these systems are that no particle size information can be obtained, and there is no way of knowing exactly how many particles are moving. The systems do not work well in streams with low sediment transport rates, where there are a limited number of collisions.

More recently, Downing et al. (2003) have been developing an acoustic sensor that records an impulse from the collision of a moving particle into a piezoelectric material. The strength of the recorded impulse is proportional to the momentum of the colliding particle. With knowledge of the particle velocity, the mass of the stone can be backed out. An inherent weakness of the system is that the instrument is an obstruction to the flow, and therefore necessarily changes the hydraulics at the measurement site. Also, since particle velocity is required to obtain mass information, the system requires an independent means of measuring, or theoretical estimation of particle velocities.

1.5.4 The Magnetic Method:

The magnetic method uses magnetic induction to detect the movement of individual particles. A detector rod is installed at a stream cross-section; as particles pass over the detector, they induced a voltage spike. The change in voltage is continuously logged producing a time series, and allowing one to count the number of particles passing over the detector through time. The method was developed by Ergenzinger and Custer (1982) at Calabria, Italy and Squaw Creek, Montana, and Reid et al (1984) at Turkey Brook, UK. Originally, particles were tagged with inserted ferrite rods. Improvements to the sensitivity of the method allowed Squaw Creek, a stream with naturally magnetic particles to be chosen.

Similar to the Birkbeck bed load sampler, there is the potential for unmanned operation with the magnetic system. Since particles are detected instead of trapped, the procedure is much less physically demanding; however, initially it was time consuming to process the number of signals recorded. With the strip chart system at Squaw Creek, Bunte (1996) manually counted voltage peaks at a resolution of 200 peaks/hr. Improvements to the system were made so that the voltages were tracked digitally (Custer, 1991). Digital recording allows computer programs to be written to process the signals. It also allows for more advanced time series analysis.

Tunnicliffe et al. (2000) have further refined the magnetic method with the Bed load Movement Detector (BMD) system, which uses high frequency recording, and much smaller detectors. In Squaw Creek, 1.55 m long detectors were installed across the creek to give an indication of the spatial variability of movement. Tunnicliffe et al (2000) installed an array of 82 sensors, each 10 cm in diameter, across O'Ne-ell Creek, British Columbia, providing high spatial resolution. Each sensor was digitally sampled at ~100Hz, increasing the temporal resolution dramatically as well. Like the setup at Squaw Creek, the BMD system is sensitive enough to detect movement of natural particles.

All of these magnetic systems are only able to detect a proportion of the sediment moving due to the mineralogy of the particles. In the case of the artificially tagged systems, the sample size was 100 stones (Reid et al., 1984). In the case of natural sediments, it was estimated that 40% of the bed material had sufficient magnetic minerals to be detected in Squaw Creek; in O'Ne-ell Creek, due to the heterogeneity of lithology and sensor spacing, 30% of the transported material could be detected. This percentage is assumed to remain constant, because there is no basis for the preferential transport of the more magnetic particles. Therefore, data collected by the magnetic method are still representative.

There are many features of the magnetic method that make it attractive: the sensors can detect the movement of natural stones; unlike pit-traps, there is no capacity limit; the system provides high resolution data in both time and space; and the system has the potential to be run unmanned. However, use of these systems has been limited due to an inadequate understanding of how to interpret the collected data. To date, the systems have been used to count the number of stones passing, and to consider temporal and spatial trends in the sensor response. No system can yet be used to produce a reliable estimate sediment transport. Spieker and Ergenzinger (1987) suggested that the magnitude of the induced voltage could be related to the size of the passing particle however, no results were produced to support the idea. Similarly, Tunnicliffe (2000) suggest that calibration of the BMD system is required to improve results.

1.6 Research Objective:

The magnetic method has great potential for sediment transport monitoring. However, its application has been limited because to date there has been no proper calibration of the method. The objective of this thesis is to test and calibrate the BMD system developed by Tunnicliffe et al. (2000) to address whether or not the magnitude of the sensor response can be related to particle size, and whether the system can be used to reliably measure the amount of sediment transport.

To accomplish this objective, Chapter 2 provides an overview of the BMD system and outlines the basic physics of the sensors. Chapter 3 describes the two methods used to test the system. Chapter 4 provides results from the experiments, and Chapter 5 discusses the results, as well as some problems that were observed with the current sensor design.

Chapter 2: The BMD Sensor:

The BMD system consists of an array of sensors housed in an aluminum beam, buried in the stream channel, flush with the bed surface. The beam can be adjusted vertically to account for scour or fill. Each sensor is digitally sampled via analogue-digital recorders. Figure 2.1 shows a schematic of the BMD system, and the system deployed in the field.

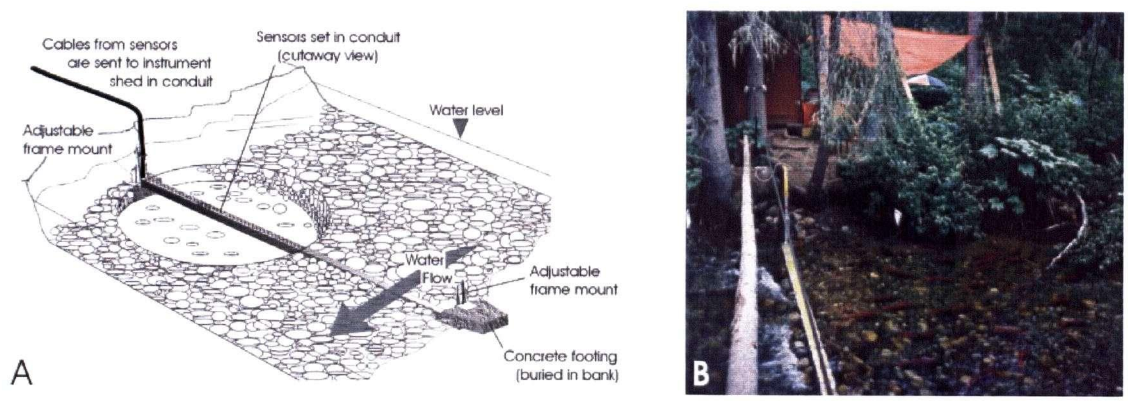

Figure 2.1. A: a schematic view of the BMD system installation, B: the BMD system deployed in O'Ne-ell Creek

In order to calibrate the system, an understanding of how an individual sensor responds to a passing stone is required. A view of the sensor is shown in Figure 2.2. The sensor is 8 cm in diameter, made of a copper coil set within a strong (~10 mT), vertically magnetized, doughnut-shaped magnet. Both are set inside a steel casing that acts to confine the magnetic field so that the fields of adjacent sensors are isolated from each other.

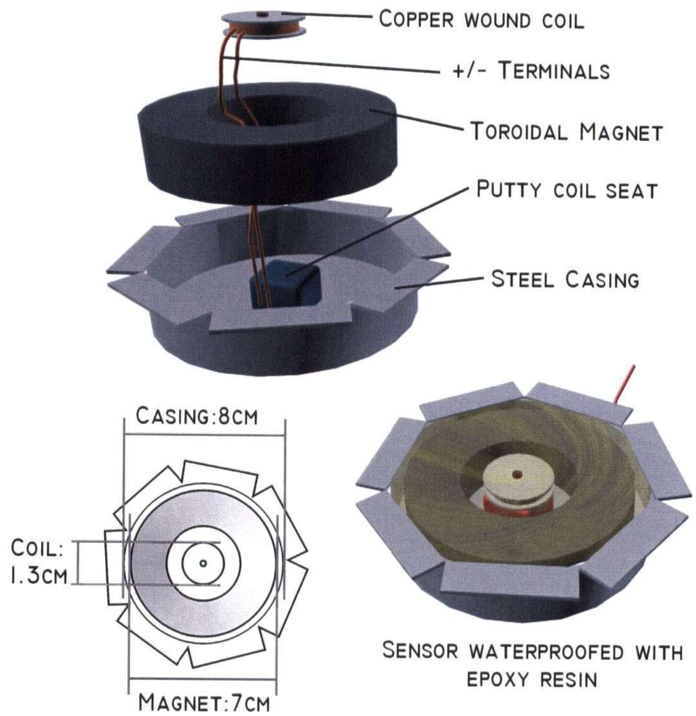

Figure 2.2. Schematic view of an individual sensor, showing the three main components: the coil, the doughnut shaped magnet, and the steel casing

2.1 Sensor Physics:

The BMD sensor works through the process of electromagnetic induction. As a particle moves over the sensor, the magnetic moments of the ferromagnetic minerals in the particle align to the magnetic field of the doughnut shaped magnet. This alignment produces an induced magnetization in the particle. As this induced magnetic field moves overtop of the sensor coil, a voltage is induced according to Faraday's Law:

$$\mathrm{emf} = -\mathrm{NA}\frac{\mathrm{dB}}{\mathrm{dt}} \tag{1}$$

which states that the induced voltage (emf) is equal to the number of coil windings (N), times the cross sectional area of the coil (A), times the change in magnetic field strength (B) with time (t). The induced voltage is measured by the analogue-digital recording system; typical recordings are on the order of 10^{-3} – 10^{-4} V.

To describe the typical sensor response, Figure 2.3A shows the simple case of a magnetic dipole moving over a coil at a number of different times. The vertical component of the magnetic field strength (B) experienced in the coil is calculated from:

$$B = \frac{\mu_o M}{4\pi}\frac{3\cos^2\theta - 1}{r^3} \tag{2}$$

where μ_o is the permeability of free space and M is the magnetization ($\mu_o M/4\pi$ in this case is constant); θ is the angle off of vertical between the center of the dipole, and the center of the coil; and r is the distance from the center of the coil to the center of the dipole. The maximum field strength occurs when the dipole is directly over the coil ($\theta = 0^\circ$), and decreases symmetrically away from the maximum, producing a Gaussian curve (Figure 2.3B). Since the number of windings (N) and the area (A) of the coil are constant, the induced voltage is directly proportional to the change in magnetic field dB/dt – the time derivative of the Gaussian curve (Figure 2.3C). This characteristic curve, with a peak followed by a valley, is recorded for each stone passing over the sensor. The shape of the curve can be described by its amplitude, width, and the area under the curve.

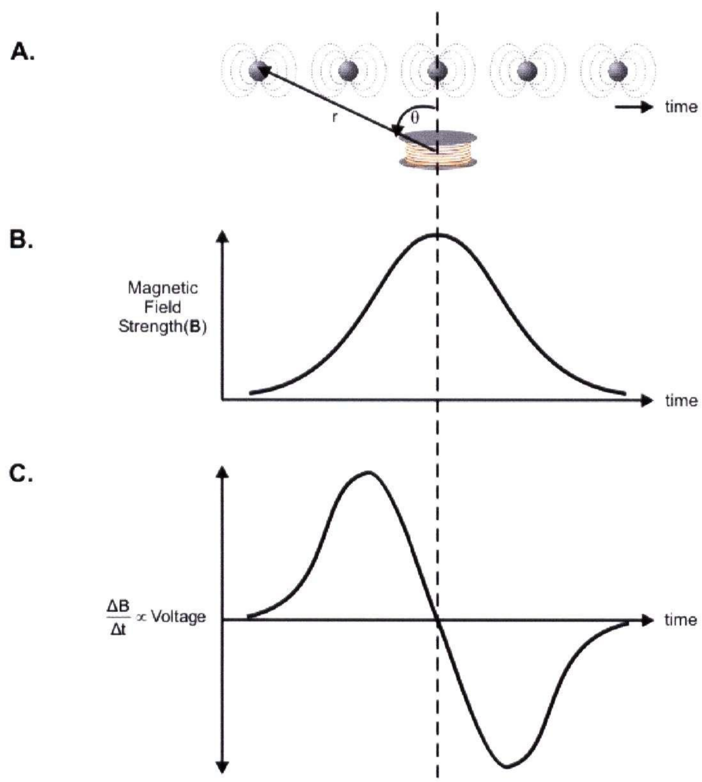

Figure 2.3. A: the simplified case of a magnetic dipole passing over a copper coil, B: the magnetic field strength (B) experienced in the center of the coil, C: the voltage response of the coil to the passing dipole, which is proportional to the derivative of the magnetic field strength with time.

2.2 Variables Controlling Sensor Response:

Though the shape of the response curve is simple to describe, the output signal of a stone passing over the sensor is controlled by a number of variables. The strength of voltage response, and the exact shape of the resulting curve, will depend on particle characteristics – velocity, size and mineralogy – and the trajectory of the particle moving over the sensor (both a horizontal and vertical component). Sensor calibration requires that each variable can be isolated to characterize its influence on the shape and size of the response curve.

2.2.1 Particle Characteristics:

From Equation 1 it is evident that a faster particle will have a greater value of dB/dt, and therefore a larger voltage response. As a particle moves into the magnetic field of the sensor, it acquires an induced magnetization (M). The strength of the magnetization can be calculated by:

$$M = \frac{B_o \chi V}{\mu_o} \tag{3}$$

where B_0 is the strength of the magnetic field from the sensor's magnet, χ is the magnetic susceptibility of the particle, and V is the volume of the particle. Therefore, the sensor response is directly proportional to particle velocity, volume and susceptibility.

Magnetic susceptibility is a unitless quantity that describes how strongly an object will respond to an external magnetic field. Susceptibility is related to the mineralogy of the particle, as it is a measure of the amount of magnetic minerals in the rock.

Each particle may also have a second magnetic property related to its mineralogy – a remanent magnetization. Remnant magnetization is a natural, inherent magnetic field due to the abundance and arrangement of magnetic minerals within the stone. Since the strength of the magnetic field is a vector, as a stone with remanent magnetization rolls over the sensor, it may distort the shape of the characteristic response, increasing the complexity of the signal.

In order to investigate these two properties, the remanence and susceptibility of 45 stones from East Creek were measured. Measurements were made at the Paleomagnetism Lab at the Pacific Geoscience Centre, in Sydney, BC, the results of which are summarized in Table 2.1.

The Koenigsberger ratio is a non-dimensional ratio of remanence to susceptibility. It is used in paleomagnetism studies as an indicator of a rock's ability to maintain a stable remanence in the presence of the earth's magnetic field. The ratio is calculated as:

$$K = \frac{NRM}{\chi \frac{B_o}{\mu_o}} \tag{4}$$

Table 2.1. Analysis of the magnetic properties of 45 East Creek stones

Sample #	Susceptibility (x10^{-6})	Remnanat Mag (A/m)	Koenigsberger Ratio
1	2.96E-01	6.32E-03	0.006
2	5.96E-01	2.36E-03	0.032
3	3.29E+00	1.11E-02	0.037
4	7.77E-04	3.25E-05	0.003
5	8.36E-02	8.52E-04	0.012
6	4.44E-03	4.03E-05	0.014
7	5.28E-01	2.95E-03	0.023
8	1.38E-02	5.14E-04	0.003
9	1.46E+00	2.51E-03	0.073
10	3.93E-04	7.04E-06	0.007
11	7.93E-02	4.45E-03	0.002
12	3.94E-01	2.41E-03	0.021
13	2.65E-01	1.28E-03	0.026
14	1.49E-01	1.01E-03	0.019
15	1.53E-01	2.49E-03	0.008
16	1.35E-03	3.51E-05	0.005
17	1.52E-01	9.22E-03	0.002
18	2.53E-01	1.47E-03	0.022
19	2.80E-03	5.61E-05	0.006
20	3.01E-01	1.09E-03	0.035
21	2.73E-01	6.49E-03	0.005
22	1.44E-01	3.86E-03	0.005
23	1.64E+00	1.23E-02	0.017
24	1.85E+00	5.05E-03	0.046
25	8.34E-01	8.49E-03	0.012
26	3.88E-02	2.60E-03	0.002
27	4.01E-02	1.57E-04	0.032
28	1.25E+00	5.00E-03	0.031
29	2.72E-01	1.63E-02	0.002
30	6.10E-03	3.24E-04	0.002
31	3.56E-01	8.80E-03	0.005
32	1.34E-02	1.16E-03	0.001
33	1.26E-02	9.52E-04	0.002
34	8.58E-04	8.33E-05	0.001
35	4.82E-04	1.34E-05	0.005
36	8.65E-01	6.55E-03	0.017
37	7.78E-02	5.20E-03	0.002
38	5.41E-01	6.48E-03	0.011
39	6.76E-01	1.26E-02	0.007
40	5.13E-03	4.94E-05	0.013
41	2.67E-01	4.14E-04	0.081
42	2.03E+01	1.52E-02	0.167
43	4.21E+00	5.24E-03	0.101
44	1.23E+00	3.91E-03	0.040
45	1.18E+00	7.16E-03	0.021

where NRM is the natural remanent magnetization, χ is the susceptibility, B_o is the local field strength in Tesla, and μ_o is the permeability of free space Henrys per metre. A ratio >1 indicates a remanence dominated sample, while a value <1 indicates an inductance dominated sample. Because of the strength of the field created by the doughnut shaped magnet (~10 mT), all the Koenigsberger ratios are well below 1, indicating that the response of the sensor is controlled by the induced magnetization, and that the effect of remanence can be ignored.

2.2.2 Particle Trajectory:

Sensor response is controlled by particle trajectory in two ways. First, the induced voltage will rapidly decrease with increasing distance between the centre of the stone, and the centre of the coil. From Equation 2, the strength of a dipole drops off as r^{-3}; for a passing stone of finite size, a response of similar magnitude is expected.

Secondly, from Equation 3, the strength of the induced magnetization is directly related to the strength of the magnetic field produced by the sensor's doughnut shaped magnet. The strength of this field was mapped using a Gauss meter, and is shown in Figure 2.4. The strength of the sensor's magnetic field varies dramatically over the sensor face. Field strength drops off sharply to the sensor edge, indicating that the steel casing does a good job of containing the field around the individual sensor. Field strength also decreases with height above the sensor; therefore a particle passing over the edge, or high above the sensor, experiences a much smaller field, and will record a proportionally smaller response. The field strength also drops sharply over the doughnut hole. This effect will be discussed further in Section 9.2.

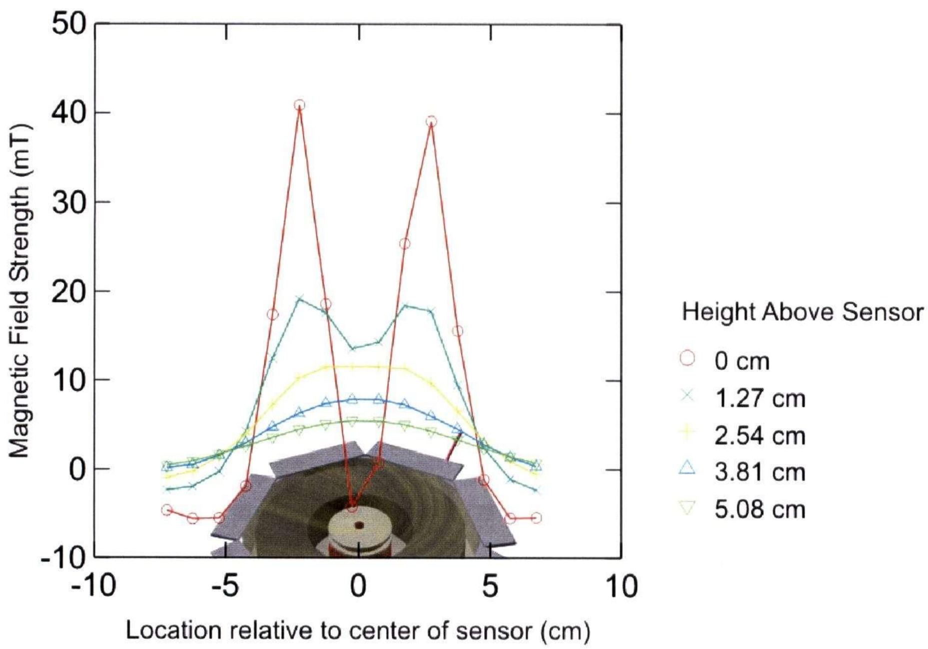

Figure 2.4. Strength of the magnetic field over the center axis of the sensor at 5 different heights

Chapter 3: Experimental Methods:

The objective of the calibration experiments was to produce a model that can be used to predict particle size from a given signal response. To build this model, two lines of experiments were designed. Rotating platter experiments were conducted to isolate individual variables, and build empirical models relating the shape of the sensor response curve and particle size. Flume experiments were conducted to test the ability to measure particle velocities, and to test the empirical models using data with more realistic particle movements.

Additional experiments were conducted with both the rotating platter and a ramp apparatus to investigate the response of multiple stones passing simultaneously, or in rapid succession, and sand pulses.

3.1 Rotating Platter Experiments:

Rotating platter experiments were designed to independently assess 5 particle variables: volume, susceptibility, velocity, and trajectory in both the vertical and horizontal.

To account for particle volume and susceptibility, artificial stones were cast using a mixture of portland cement, sand and iron filings. Four different mixtures were used, and are summarized in Table 3.1. For each mixture, 8 size classes were cast, representing 8, 11, 16, 22, 32, 45, 64 and 90mm size classes (Figure 3.1).

Table 3.1. Mixture ratios (by mass) for the artificial stones

Mixture #	Sand (%)	Cement (%)	Iron Filings (%)	Average Susceptibility
1	75	20	5	1600
2	70	20	10	3200
3	65	20	15	4800
4	60	20	20	6400

Figure 3.1. Artificial stones cast in 8 class sizes from 8 – 90 mm

To account for particle trajectory and velocity, a rotating platter was designed (Figure 3.2). Two sensors were located above a rotating styrofoam platter, facing down. Particles were placed on the platter at known radius from the center pole, and passed by the sensor. The styrofoam platter could be adjusted vertically to vary the distance of the particle from the sensor, and the sensors moved along a track to vary the horizontal location of the particle across the sensor face. Platter rotation was powered by a 4-speed turntable. Experiments were conducted at approximately 0.60, 1.15, 1.50 and 2.40 m/s, spanning the range of particle velocities that we might expect in the field (Bridge and Dominic, 1984).

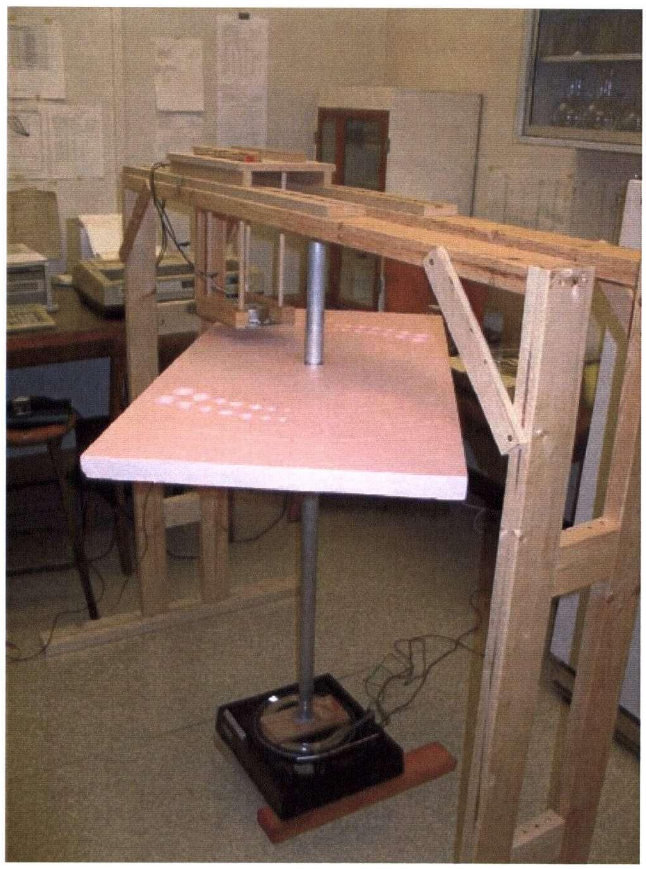

Figure 3.2. Rotating Platter apparatus, designed to independently control particle trajectory (both vertical and horizontal) and particle velocity.

A ramp apparatus was also used in later experiments. This apparatus was mainly used to record pulses of sand, and groups of particles, which could not be accommodated by the rotating platter apparatus. Two sensors were inset in a piece of wood that acted as a ramp (Figure 3.3). Adjustable sidewalls were used to confine the passage of the particles over one individual sensor.

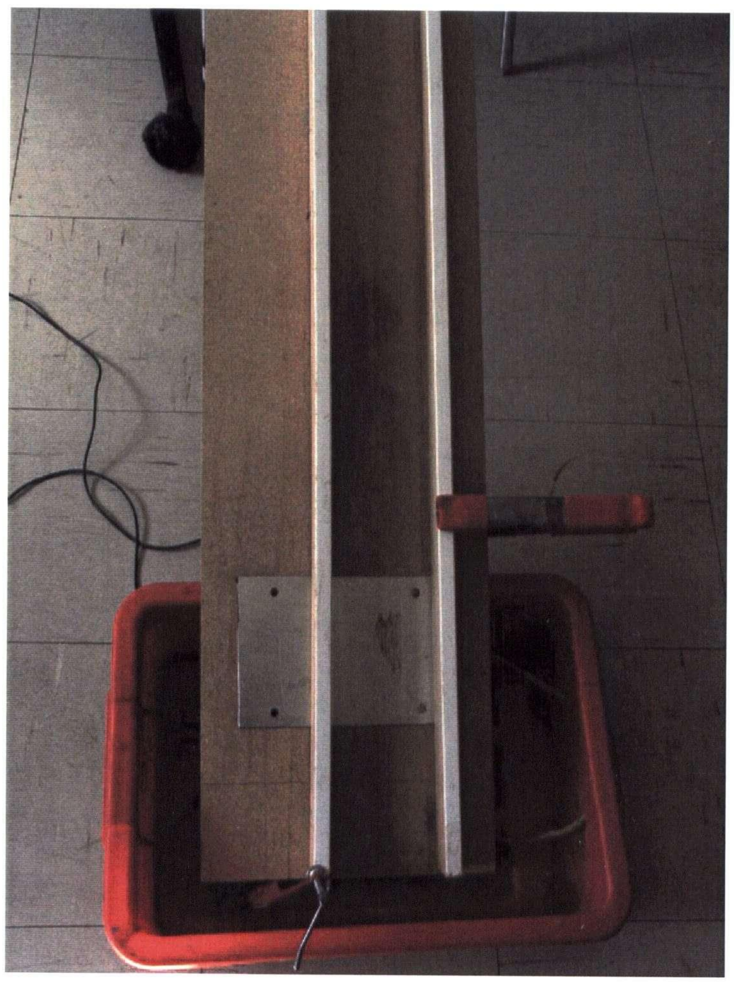

Figure 3.3. Ramp apparatus. Two sensors are inset into the ramp; adjustable sidewalls confine particles over a given sensor.

3.2 Flume Experiments:

After the rotating platter experiments, flume experiments were conducted to produce more realistic simulation of particle movements, and to test the use of the BMD system to measure particle velocities. Figure 3.4 shows the flume set-up, looking upstream from the sensors. The flume was 45 cm wide, and 6 m long. A fixed bed was produced by gluing stones to a plywood sheet with fibreglass resin. The flume slope was set to 1%. Two rows of 4 sensors each spanned the width of the flume, with 22 cm separating the rows. Initially the fixed bed continued immediately downstream of the sensor rows; however, due to the sharp changes in bed roughness from the fixed bed to the smooth aluminum plate of the sensors, and back to the fixed bed, a standing wave developed overtop of the second row of sensors. The wave slowed particle movement, and even stopped the movement of 8 mm particles. To overcome this problem, the bed was kept smooth for a section downstream of the sensors, which had the effect of pushing the standing wave downstream, allowing uninhibited movement of the particles over the sensors.

Two rows of sensors were used in these experiments to test the ideas of Spieker and Ergenzinger (1987) who suggested that the velocity of an individual particle could be analyzed through the time lag in the voltage response between the two rows. The experiments were also recorded with an overhead video camera, which was used as a second method of tracking particle velocities. Experiments were run at 5 different discharges (11, 17, 22, 27 and 33 L/s) to produce a range of particle velocities.

The same artificial stones from the rotating platter experiments were also used in the flume experiments. Stones were fed into the flume one by one. Initial experiments used single size classes from a single cement mixture. In later experiments, the complexity was increased by adding multiple size classes from one cement mixture, multiple cement mixtures from one size class, and a complete mix of sizes and cement mixtures.

Figure 3.4. Flume set-up. Two rows of 4 sensors each are visible in the foreground. The coloured stones are the artificial stones used for these experiments.

3.3 Data Collection and Signal Processing:

The resulting data from each experiment is a set of voltage time series. Each sensor is connected to an individual channel on an analogue-digital recorder. In the initial field deployment, Tunnicliffe et al. (2000) recorded at 104 Hz; in the calibration experiments, the sensors were sampled at 501 Hz. The choice of sampling frequency is a trade off between adequately capturing the signal, and storage space for the digital data. Data storage technology has improved significantly in the past few years, allowing for higher frequency recording.

LabView software was used in order to process and analyze each time series. The raw time series includes information about both the passing particles and background noise. LabView offers a number of built in filtering features from which a low-pass Butterworth filter was selected to block out the background noise. The low-pass filter allows data with frequency content below a specified threshold to pass, while blocking any data with frequency content above the threshold. Figure 3.5 shows the effect of filtering the same signal at a number of different thresholds. The faster particles have higher frequency content, and begin to get filtered out at higher thresholds. If the threshold is set too low, then some of the true signal gets filtered out, and the response diminishes, but if the threshold is too high, too much background noise gets through, increasing the minimum detection threshold above the noise. For analysis of the calibration experiments, a filter threshold of 55 Hz was chosen, as it represents a good balance of filtering out noise, without losing actual signal. Figure 3.6 shows the same time series before and after filtering.

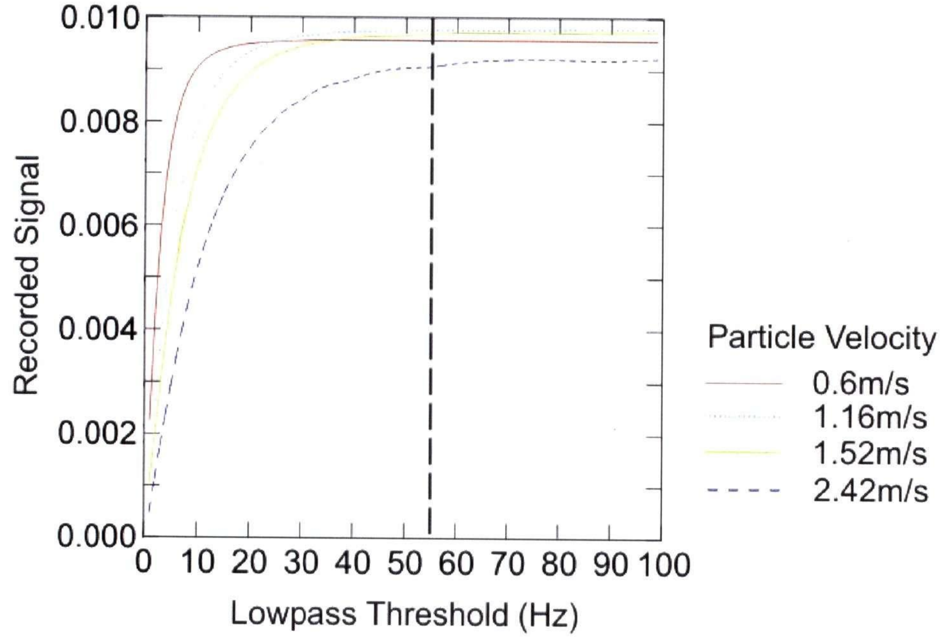

Figure 3.5. The effect of filter threshold on the recorded signal – too low of a threshold causes data to be lost. A 55 Hz filter was chosen for the current analysis.

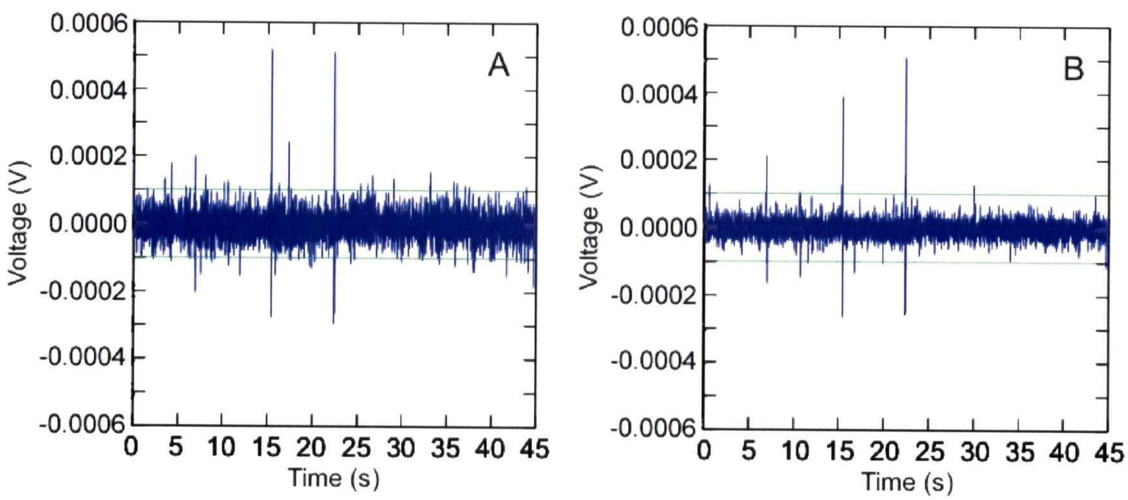

Figure 3.6. A: Raw data with no filtering. B: Data after filtering with 55 Hz lowpass filter. The horizontal lines represent the noise range of the system after filtering.

After filtering, individual responses were identified. Because of the characteristic shape of the response curve, LabView's peak detection sequence was suitable for identifying individual signals. With the peak detection sequence, a minimum response threshold of 1×10^{-3} V was used, which represents the noise in the recording system (see Figure 3.6). Individual particles were identified from other random noise by detecting pairs of peaks and valleys. As shown in Figure 3.7, each signal was characterized by its amplitude, width, and area under the curve. Signal width was calculated as the time difference between the peak and the valley. The integration of the curve was calculated as the average of the area under the peak and the area under the valley from zero crossing to zero crossing, using the trapezoidal rule. The minimum signal integral that could be calculated was 2×10^{-6} V*s.

The area under the peak from a given signal is equal to the amplitude of the integral of the signal; therefore, a simpler way to calculate the area under the curve would have been to use the built-in integration feature in LabView to integrate the time series, and then to use a second peak detection sequence. This was attempted however there was low frequency noise that would confound the signal. A high pass filter was used to try to block out this noise, but the frequency range of the noise was not consistent between time series, making it difficult to automate the data processing.

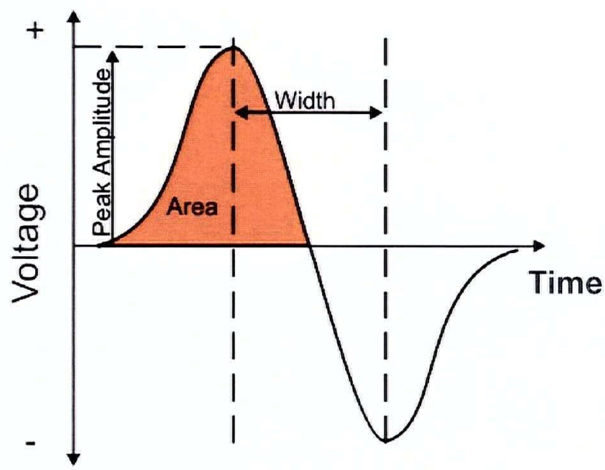

Figure 3.7. Signal parameters collected from each sensor response.

Chapter 4: Results and Analysis

4.1 Particle Characteristics:

Initial experiments using the rotating platter apparatus were designed to investigate the relationships between sensor response and particle size, susceptibility and velocity. For these experiments, a constant trajectory over the center of the sensor was used.

From the data collected in these experiments, empirical models can be built to solve the inverse problem: given a signal response, what is the particle size? The models are developed for maximum possible sensor response (i.e. particles passing in contact with, and directly over the center of the sensor face), and a known susceptibility. Models are developed for each signal parameter: amplitude, width and integral.

4.1.1 Signal Amplitude Results:

The signal amplitude will be controlled by all three variables (size, susceptibility and velocity). From Equations 1 thru 3, increasing the particle susceptibility or volume will increase the induced magnetization, thereby increasing B and the peak voltage response. Increasing particle velocity will act to increase dB/dt, also increasing the amplitude.

The relation between particle volume and signal amplitude is shown in Figure 4.1. The log-log plot shows data for stones from a single susceptibility (1600), sorted by particle velocity (RPM). The data follow a linear trend on the log-log plot, indicating a power relationship. There is a consistent break in slope near 12

cm^3, above which the relation is less steep, suggesting that above this volume the top portion of the stone does not contribute as strongly, due its distance from the sensor.

Figure 4.2 shows the relation between particle velocity and signal amplitude. The plot shows data from a single susceptibility (1600), sorted by size class. The slope of the power relation appears to increase as particle size increases.

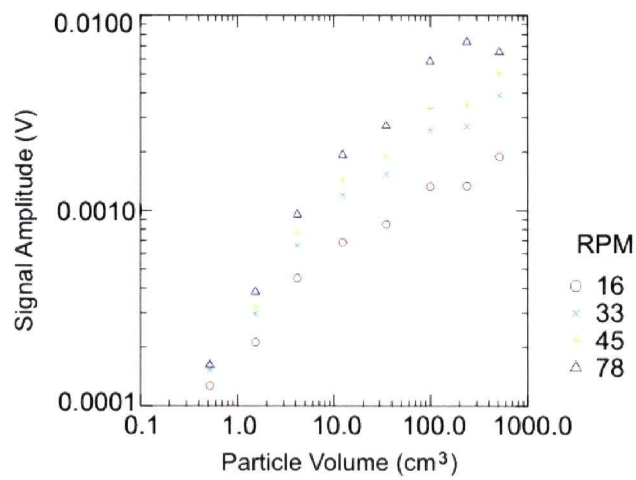

Figure 4.1. Relation between particle volume and signal amplitude. The slope of the relation increases with increasing RPM. There is a consistent break in slope near 12 cm^3, above which the slope decreases.

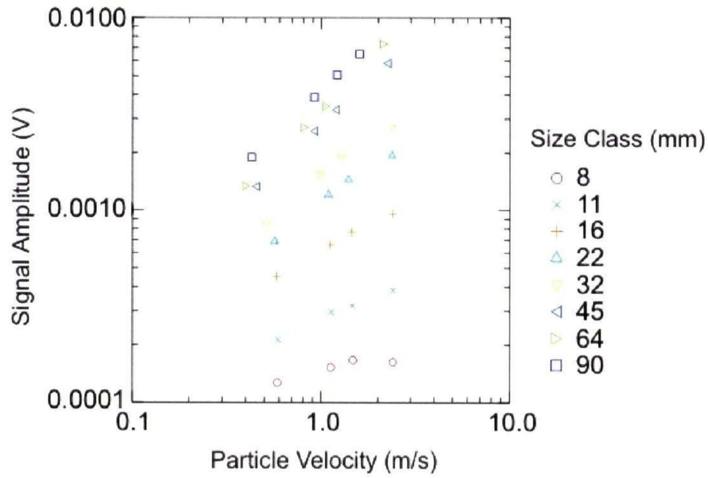

Figure 4.2. Relation between particle velocity and signal amplitude. The slope of the power relation increases as particle size increases.

The relation between particle susceptibility and signal amplitude is shown in Figure 4.3. The data are from one particle velocity (33 RPM), sorted by particle size, with susceptibility plotted on an arithmetic axis, and signal amplitude plotted on a log axis. Again, the data follow a positive linear trend.

Combining all 3 variables, Figure 4.4 is a 3-dimensional log-log-log plot with volume, velocity and amplitude plotted on the x,y and z axes respectively. The data are sorted by susceptibility. For a given susceptibility, the data fall on a plane through the space. The plane shifts up the amplitude axis as susceptibility increases.

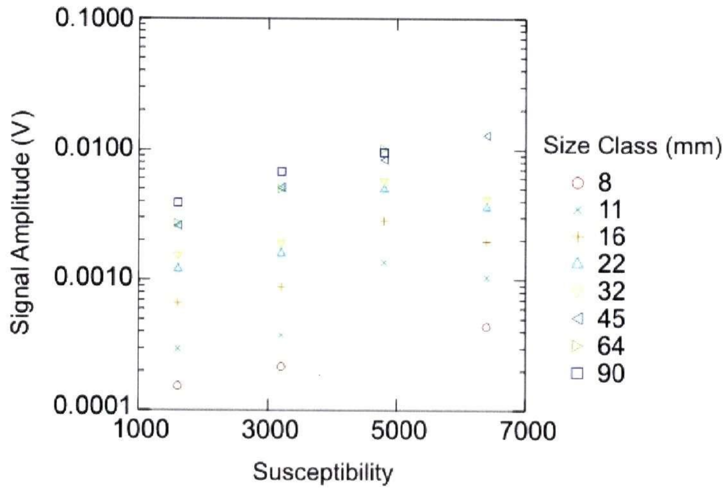

Figure 4.3. Semi-log relationship between susceptibility and signal amplitude.

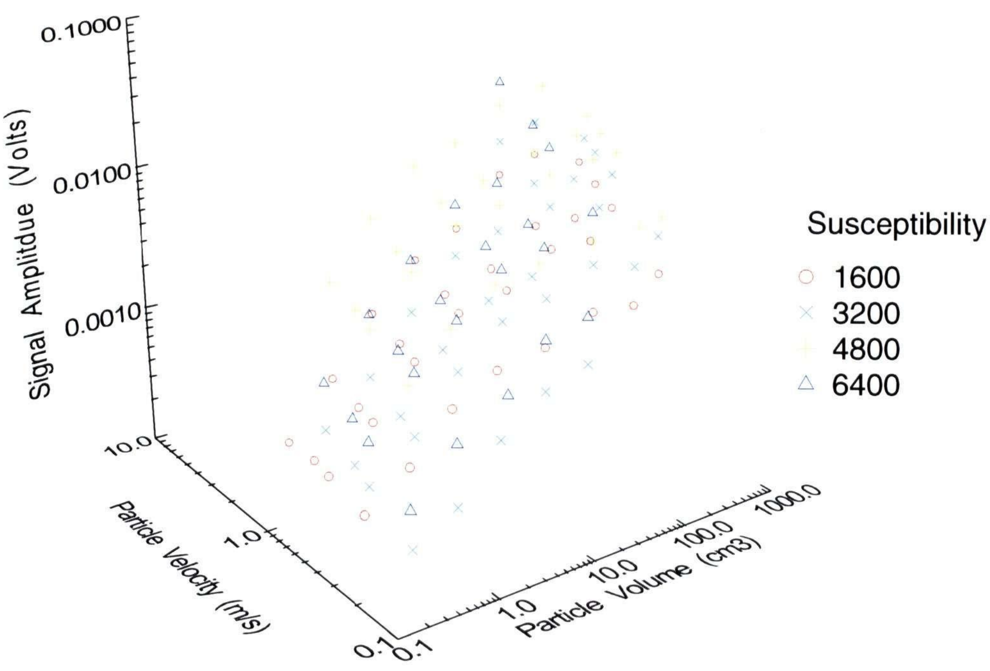

Figure 4.4. 3-dimensional plot of the variables affecting signal amplitude. For a given susceptibility, the points fall along a plane through the amplitude-velocity-volume space.

4.1.2 Empirical Model for Signal Amplitude:

Taking the results from Figure 4.4, the data was run through multiple regression to produce a relationship of the form:

$$\log(A) = c + b_1[\log(V_p)] + b_2[\log(v)] + b_3[S] + \varepsilon \qquad (6)$$

where A is amplitude in Volts, V_p is particle volume in cm^3, v is particle velocity in m/s, S is susceptibility in SI units per m^3, c is the regression constant, b_i are the regression coefficients, and ε is the error. As discussed in Section 4.1.1, there is a break in slope in the data at approximately 12 cm^3. Separate regressions were run for data above and below this threshold. The results of the regressions are summarized in Table 4.1. The high R^2 values are somewhat misleading because of the log transformations.

Table 4.1. Regression coefficients for the amplitude model. Separate regressions were run for stones <12 cm^3 and >12 cm^3.

	Volume < 12cm^3		Volume > 12cm^3	
	Coefficient	Standard Error	Coefficient	Standard Error
c	-3.87	0.029	-3.47	0.037
b_1	0.68	0.023	0.32	0.015
b_2	0.71	0.043	0.90	0.032
b_3	1.50×10^{-4}	7×10^{-6}	1.44×10^{-4}	5×10^{-6}
R^2	0.96		0.96	

Equation 6 can be rearranged to solve for particle volume:

$$V_p = 10^{\left[\frac{\log(A) - b_2[\log(v)] - b_3[S] - c}{b_1}\right]} \qquad (7)$$

Equation 7 was used to back-calculate an estimate of particle volume from the same data. Figure 4.5 shows the estimated volume results versus the actual volumes. The results are shown with both arithmetic and logarithmic axes. The logarithmic graph was produced in order to clearly show the results for the smaller volumes. The y-scale of the logarithmic plot is divided into size class regions. The regions were determined by calculating the volume of a sphere for each of the size classes (8, 11, 16, 22, 32, 45, 64, 90 mm). The median error in volume estimation is 29%, with a maximum error of 132%. Including this error, however, it is evident from the logarithmic plot that the estimates still generally fall within the appropriate size classes.

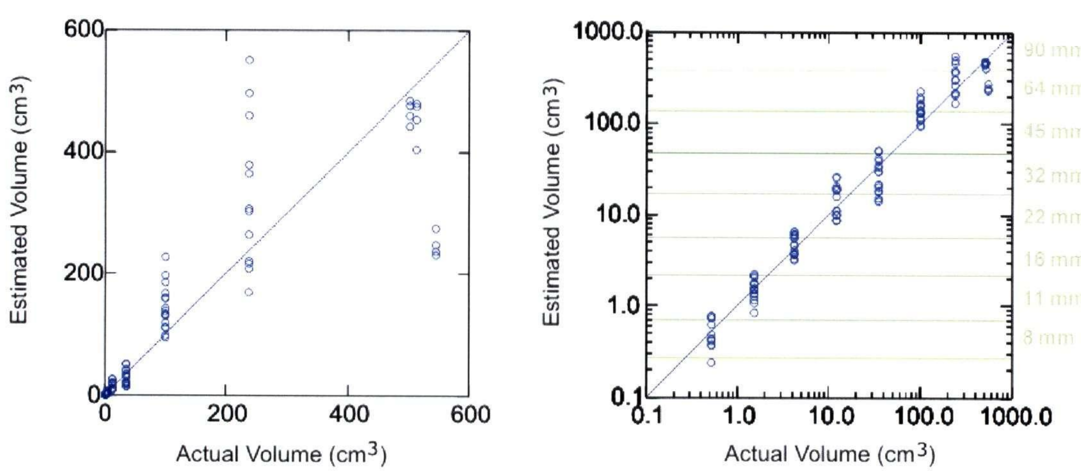

Figure 4.5. Estimated particle volumes from the empirical model versus actual particle volumes. The logarithmic plot is used in order to show the variability for each particle size clearly. The green lines divide the graph into size classes. Including the scatter about the 1:1 line, data still generally fall within the correct size class.

4.1.3 Signal Width Results:

Signal width is a measure of the length of time it takes the particle to pass over the sensor. This should be a function of both the particle velocity and the diameter of the passing stone. Since it is only a function of position and time, it should be independent of the particle susceptibility, eliminating one of the variables.

The relation between the diameter of the B-axis and signal width is shown in Figure 4.6. The plot shows data pooled from all 4 susceptibilities, at a single particle velocity of approximately 1.15 m/s. Though there is some scatter, the data follow a positive trend.

Figure 4.7 shows the relation between particle velocity and signal width. The plot shows data pooled from all 4 susceptibilities, sorted by size class. There is a negative linear trend – as velocity increases, signal width decreases. Though there is scatter, there is segregation of particle size. For a given velocity the signal width increases with particle size.

A 3-dimensional plot is shown in Figure 4.8, with velocity, B-axis diameter and signal width plotted on the x, y and z axes respectively, all in log space. The data fall nicely on a plane through this space.

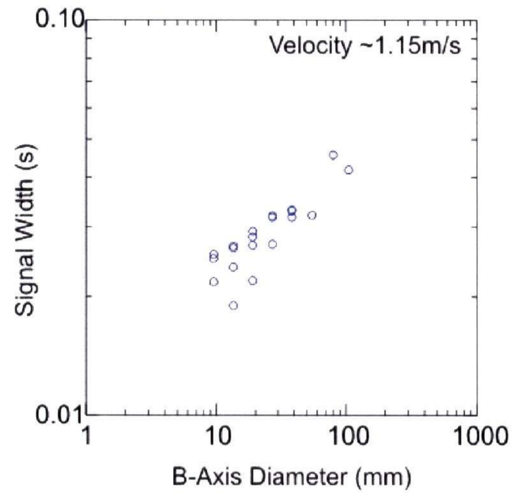

Figure 4.6. Relationship between particle diameter and signal width.

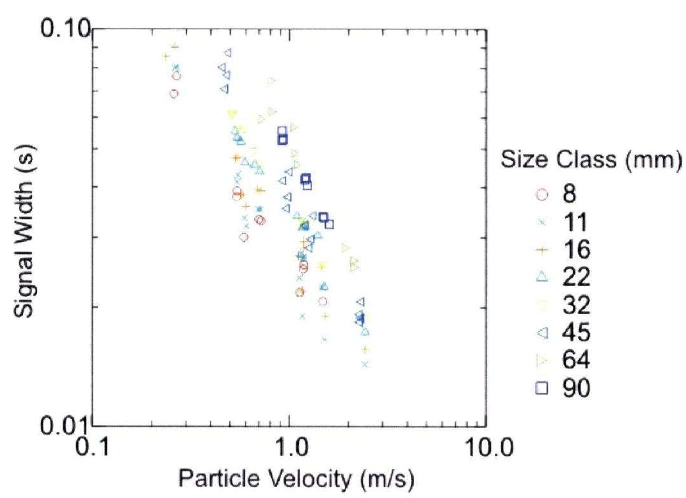

Figure 4.7. Relationship between particle velocity and signal width. There is overlap, but in general for a given velocity, width increases as particle size increases.

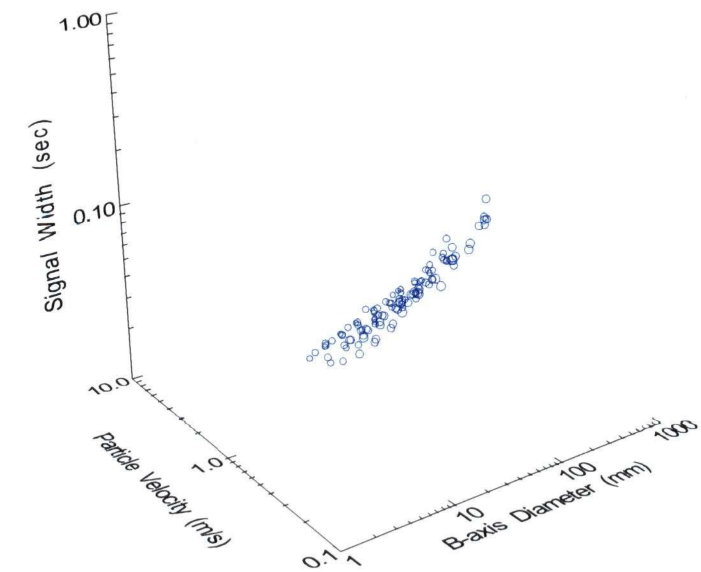

Figure 4.8. 3-dimensional plot of the variables influencing signal width. The data fall nicely on a plane within this space.

4.1.4 Empirical Model for Signal Width:

Using the data from Figure 4.8, multiple regression analysis was run with signal width (W) in seconds, B-axis diameter (D) in mm, and particle velocity (v) in m/s to produce:

$$\log(W) = -1.96 + 0.33\log(D) - 0.83\log(v) \tag{8}$$

This equation can be rearranged to solve for B-axis diameter:

$$D = 10^{\left[\frac{\log(W)+0.83[\log(v)]+1.96}{0.33}\right]} \tag{9}$$

Equation 9 was used to back-calculate an estimate of the B-axis diameter from the same data. Figure 4.9 shows the estimated versus the known diameters. With this model, the median error is 21%, with a maximum error of 106%. However, this model does not predict as well as the amplitude model; the data do not follow a general linear trend about the 1:1 line, and there is significant overlap between the different size classes so that predictions may be 3-4 size classes in error.

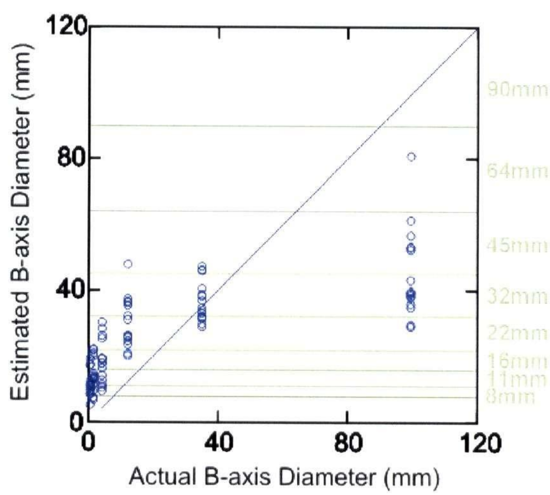

Figure 4.9. Estimated B-axis diameter from the empirical model versus actual B-axis diameter. The green lines identify the different size class regions. Scatter in the estimations span 3-4 size classes.

4.1.5 Signal Integral Results:

The area under the curve will depend on both the susceptibility and volume of the particle, but it is independent of particle velocity. From Equation 1, if the same object passes the sensor at two different speeds, the response to the faster pass will have higher amplitude and narrower width. Figure 4.10A shows the same object passing the sensor over a large range of velocities (as seen by the range in amplitudes); Figure 4.10B shows the integration of the same time series. The amplitude of the integral (which is equivalent to the area under the curve of the raw data) is the same for all signals, independent of the object's velocity. This can also be proven mathematically:

$$\int_{-\infty}^{0} \frac{dB}{dt} dt = \int_{-\infty}^{0} \frac{dB}{dx} \frac{dx}{dt} dt = \int_{-\infty}^{0} v \frac{dB}{dx} dt = \int_{-\infty}^{0} v \frac{dB}{dx} \frac{dx}{v} = \int_{-\infty}^{0} \frac{dB}{dx} dx \qquad (5)$$

From Equation 1, the number of windings (N) and the area (A) of a given coil are constant; therefore the induced voltage is directly proportional to dB/dt. The area under the curve then is proportional to the integral of dB/dt with respect to time. Equation 5 rearranges this integral to show that velocity cancels out, and that the sensor response is related to position and time independently.

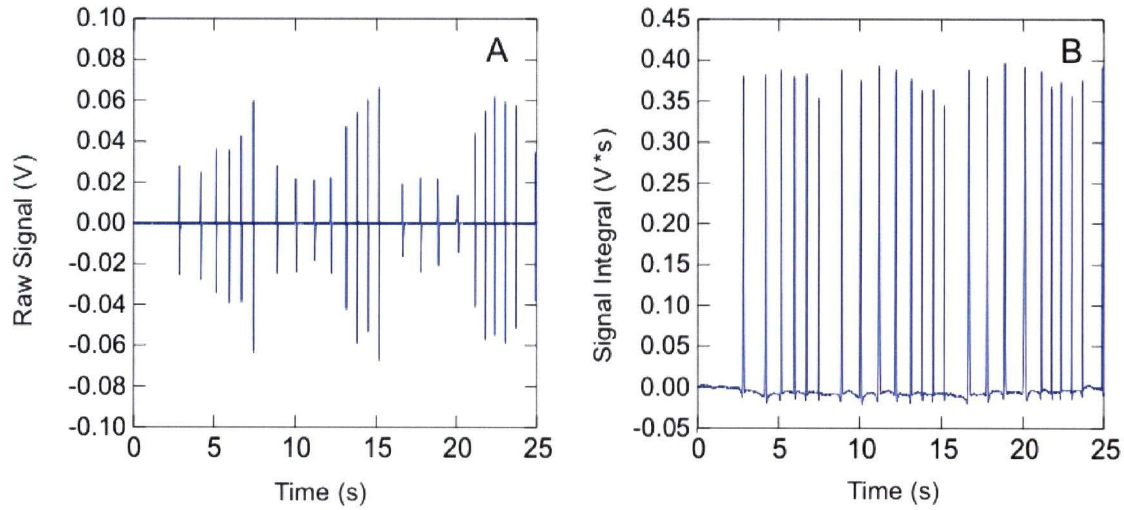

Figure 4.10. A: Time series of a single object passing by the sensor at different velocities (as seen by the difference in amplitude). B: Integral of the same time series. The amplitude of the integral is approximately the same, regardless of velocity

The relation between susceptibility and signal integral is shown in Figure 4.11. The data include the range of particle velocities, sorted by particle size, with susceptibility plotted on an arithmetic axis, and signal amplitude plotted on a log axis. The data follows a positive linear trend.

Figure 4.12 shows the relation between particle volume and signal integral. The plot includes data over the range of particle velocities, sorted by susceptibility. The linear trend again indicates a power relation. The graph is very similar to Figure 4.1; a break in slope is evident above $12cm^3$.

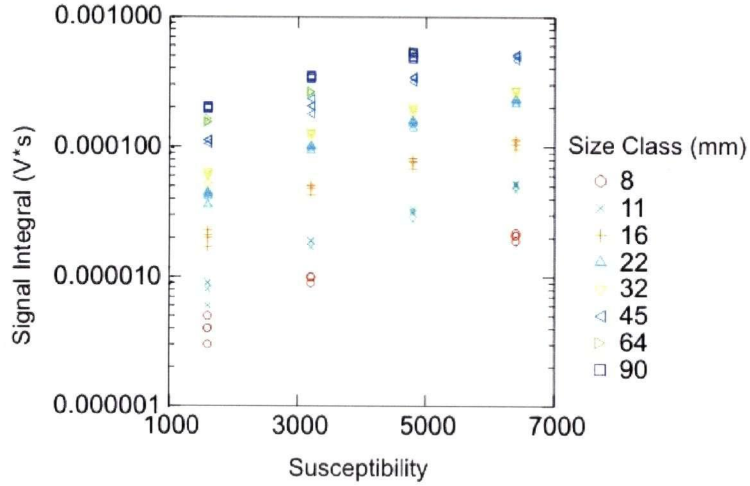

Figure 4.11. Relationship between susceptibility and signal integral

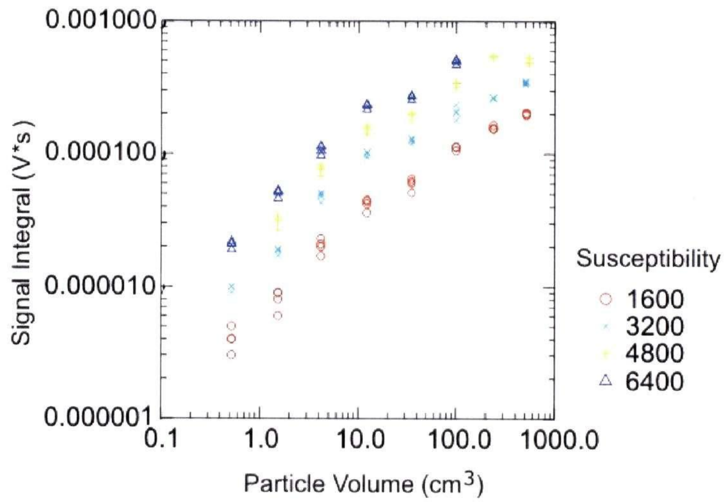

Figure 4.12. Relation between particle volume and signal integral. There is good segregation between susceptibilities. Like the relationship between volume and amplitude, there is a break in slope near 12 cm^3

4.1.6 Empirical Model for Signal Integral:

Using the data from Figure 4.12, a multiple regression model was also built for signal integral. This regression takes the form:

$$\log(I) = c + b_1[\log(V)] + b_2[S] + \varepsilon \tag{10}$$

where I is the signal integral with units V*s. In the same manner as the amplitude model, separate regressions were run for data above and below a threshold volume of 12 cm^3. The results of the regressions are summarized in Table 4.2. Again, the high R^2 values are somewhat misleading because of the log transformations.

Table 4.2 Regression coefficients for the integral model. Separate regressions were run for stones <12 cm^3 and >12 cm^3.

	Volume < 12cm^3		Volume > 12cm^3	
	Coefficient	Standard Error	Coefficient	Standard Error
c	-5.39	0.024	-4.97	0.032
B_1	0.77	0.019	0.39	0.013
B_2	1.52×10^{-4}	5×10^{-6}	1.40×10^{-4}	4×10^{-6}
R^2	0.98		0.96	

Rearranging equation 10 to solve for volume produces:

$$V = 10^{\left[\frac{\log(I) - b_2[S] - c}{b_1}\right]}, \tag{11}$$

which was used to back-calculate an estimate of particle volume from the same data. Figure 4.13 shows the estimated versus the known volumes. The results are shown with both arithmetic and logarithmic axes in order to clearly show the results for the smaller volumes. Like Figure 4.5, the y-scale of the logarithmic plot is divided into size class regions. With this model, the median error in estimation is 13%, with a maximum error of 89%. Similar to the amplitude model, even with the errors, estimates generally fall within the appropriate size class region.

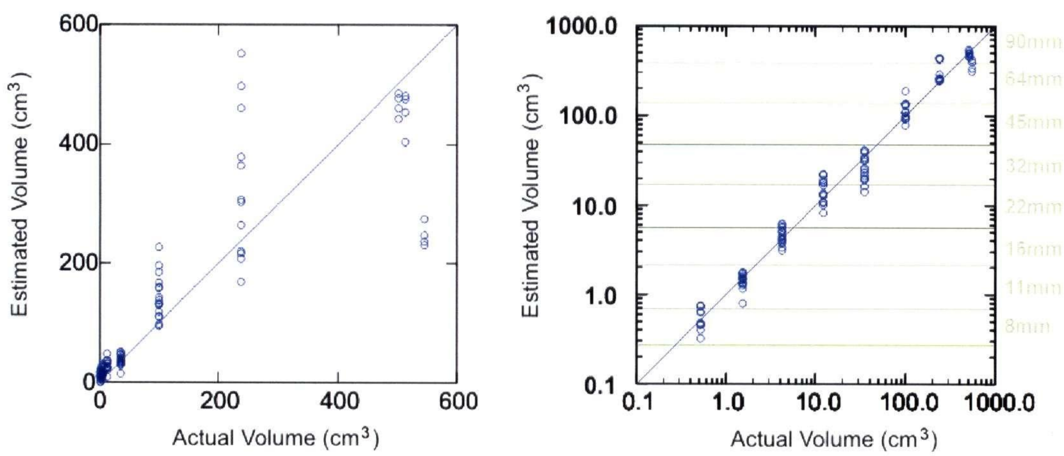

Figure 4.13. Estimates of particle volumes from the integral empirical model versus actual volumes. The green lines on the logarithmic plot divide the y-axis into size classes. Variability about the 1:1 line generally is within the correct size class.

4.2 Particle Trajectory:

The empirical models developed above are for the simplified case of particles passing over the center of the sensor, directly in contact with the sensor face. A second set of rotating platter experiments addressed particle trajectory by incrementally varying the location across the sensor face and the distance of the stone above the sensor face.

4.2.1 Variation Across the Sensor Face:

Figure 4.14 shows how signal amplitude varies across the sensor face, for 3 different grain sizes at the same velocity (78 rpm). The curve is symmetric, with the strongest response occurring over the center of the sensor, and dropping off sharply to the edge of the sensor.

The data were normalized by taking the ratio of the amplitude at a given location to the amplitude recorded over the center of the sensor. Since the data are symmetric about the center of the sensor, the relation between the absolute value of location and the normalized response is shown in Figure 4.15. There is a fair amount of spread in the data, but the relationship can be described by a line. The intercept of the line necessarily goes through one since the normalized response is unity at a location of zero; the response drops off to zero at a location of approximately 5.5cm. The equation of the line is therefore:

$$A_{Norm} = (-\frac{1}{5.5})\,|\,x\,|+1 \qquad (12)$$

where A_{Norm} is the normalized amplitude. A_{Norm} represents the percentage of the maximum possible voltage that was actually recorded.

The variation in signal integral across the sensor face is shown in Figure 4.16. The plot includes 3 different grain sizes at the same velocity (78 RPM). The curve is very similar to that of the signal amplitude. Using the same logic as above, the signal integral data were also normalized, and are plotted against the absolute value of location in Figure 4.17. This data can be described by the exact same function as the amplitude data, by substituting I_{Norm} for A_{Norm} in equation 12.

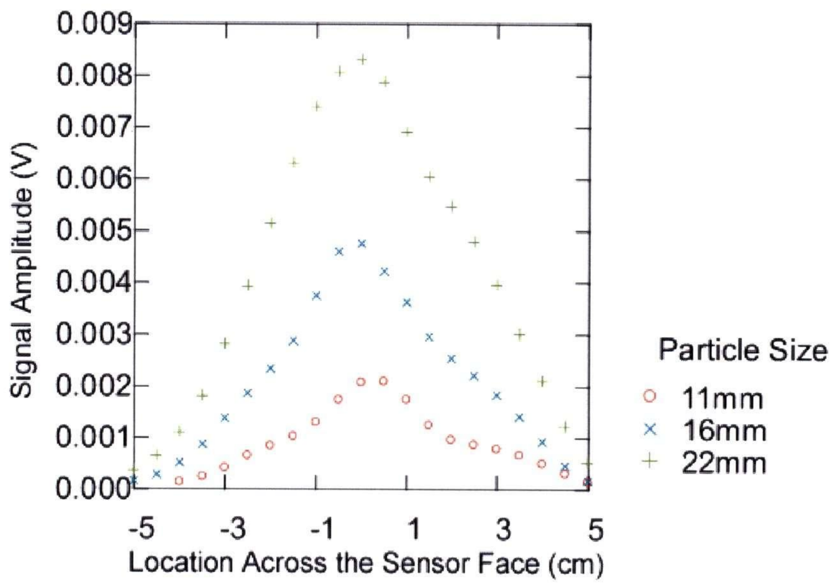

Figure 4.14. Variation in signal amplitude across the sensor face.

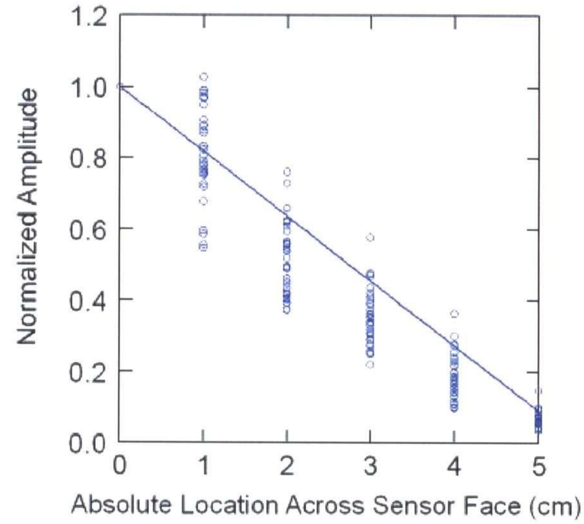

Figure 4.15. Normalized signal amplitude across the sensor face

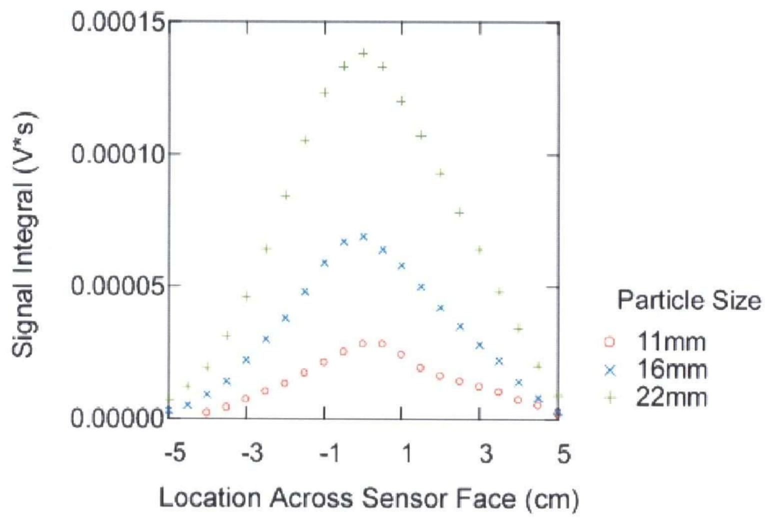

Figure 4.16. Variation in signal integral across the sensor face

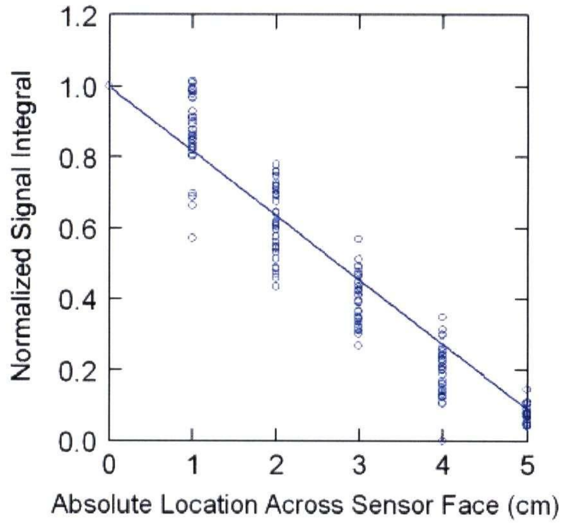

Figure 4.17. Normalized signal integral across the sensor face

The relation between signal width and location across the sensor face is shown in Figure 4.18. Again the data are from 3 different grain sizes at the same velocity. This curve is very different from that of the amplitude and integral. The response is still symmetric about the center of the sensor, but in this case, the signal width is smallest over the center of the sensor. It increases to about 2 cm from the center, before it drops off toward the sensor edge.

The results for width across the sensor were somewhat surprising. It was expected that the largest width would occur over the center of the sensor, since that is where the stone passes over the maximum sensor diameter. The results suggest that the magnetic field produced by the doughnut shaped magnet affects these results, as the locations of maximum width coincide with the edge of the doughnut hole. No normalization was attempted with the width results due to their anomalous behaviour.

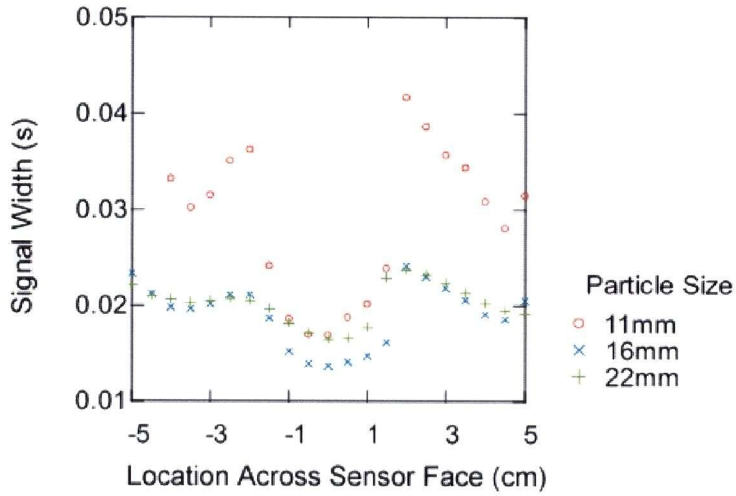

Figure 4.18. Variation in signal width across the sensor face

4.2.2 Variation With Distance From the Sensor Face:

The signal amplitude drops off as the distance between the center of the stone and the center of the sensor coil increases, as shown in Figure 4.19. The plot uses data from a single speed (33 RPM), sorted by particle size. The relation shows a general linear trend that is similar between particle sizes. At small distances the relation bends, which is likely due to the high variability in magnetic field strength close to the sensor due to the doughnut shaped magnet (see Figure 2.4). The relation between signal integral and distance between the center of the stone and the center of the coil is very similar, and is shown in Figure 4.20.

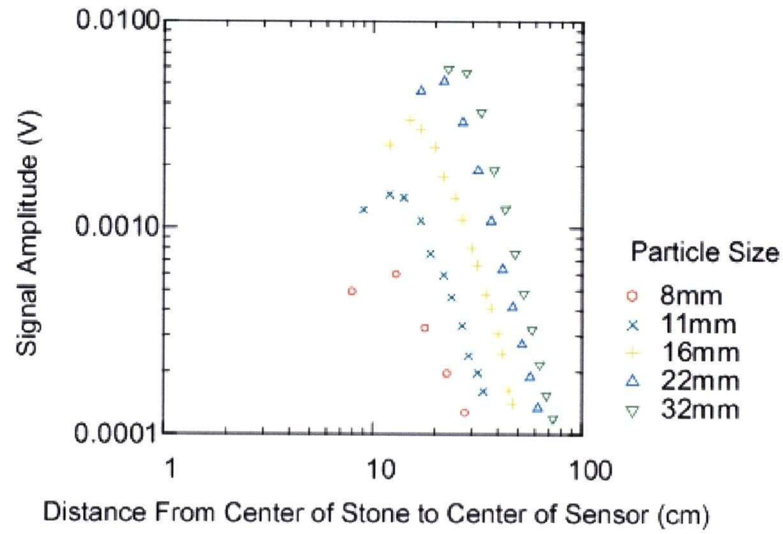

Figure 4.19. Variation in signal amplitude with increasing distance between the center of the stone and the center of the sensor

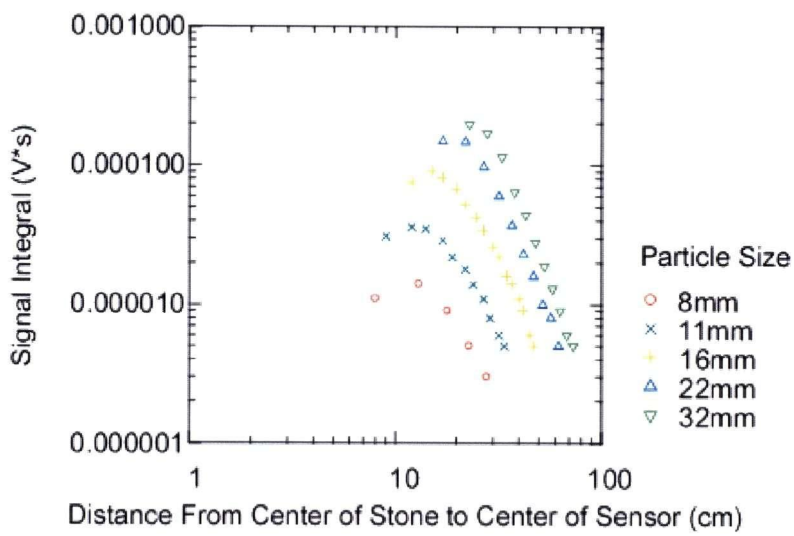

Figure 4.20. Variation in signal integral with increasing distance between the center of the stone and the center of the sensor

A plot of signal width and distance between the center of the stone and the center of the sensor coil is shown in Figure 4.21. Like the previous figures, the data are from a single velocity (33 RPM), sorted by particle size. The relation is very different from that of the amplitude and integral; in this case there is a positive relation – signal width increases with height. The slope of the relation is similar for the different particle sizes. The increase in width with height is likely due to the steel yoke that the sensor sits in. The yoke attracts the field lines, confining the field near the sensor face. As distance increases from the sensor face, however, the field lines are less affected by the yoke, allowing the stone to remain in the field for a longer duration.

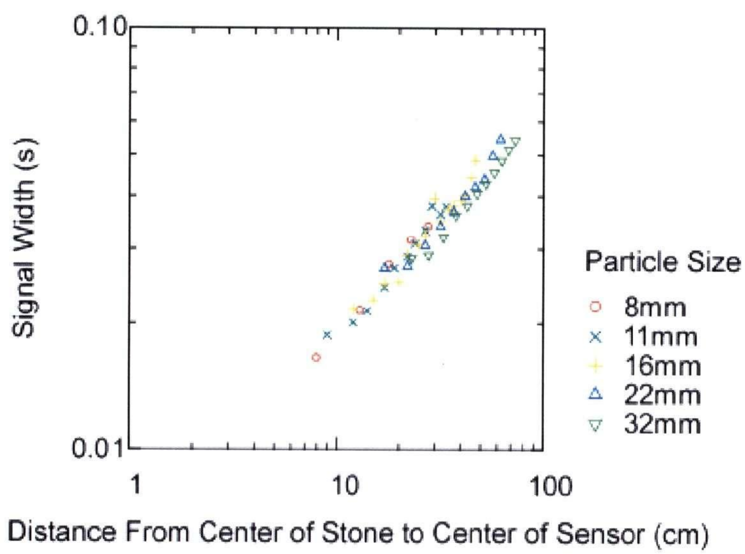

Figure 4.21. Variation in signal width with increasing distance between the center of the stone and the center of the sensor

4.3 Incorporating Trajectory into the Empirical Models:

In the field case, the trajectory of a given particle passing over the sensor will not be known; most particles will not pass directly over the center of the sensor. Because of how quickly the sensor response drops off both to the edge, and above the sensor, this adds a significant amount of complexity.

A simplifying assumption can be made that all particles will pass in contact with the sensor face (i.e. that particles are not saltating when they pass by the sensor). This was the case in the flume experiments, and is a reasonable assumption for the gravel size fractions that the sensor is able to detect. With this assumption the effect of height above the sensor can be ignored.

The effect of location across the sensor face, however, is more complex. Flume experiments were run in order to simulate more realistic particle trajectories over the sensor. In these experiments, each particle had an equal probability of passing over any location across the sensor array. To illustrate the effect that location across the sensor has, the empirical model for the signal integral was used to estimate particle volumes from the flume data. These results are shown in Figure 4.22. If the model was successful, the data should fall along the 1:1 line; without accounting for location across the sensor, the model significantly underestimates particle volumes.

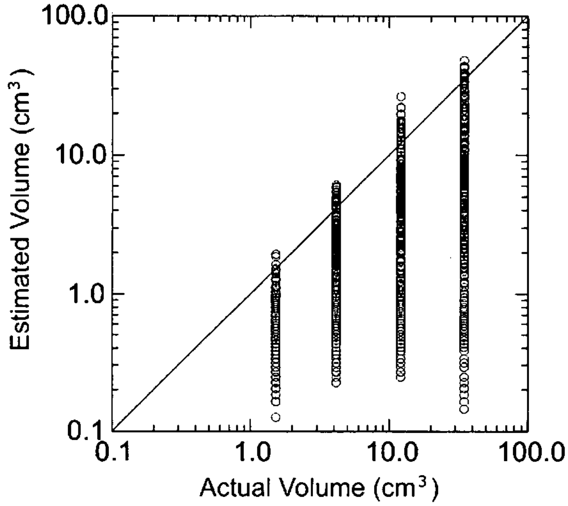

Figure 4.22. Estimated particle volumes from flume experiments with no adjustment for location across the sensor face.

One way to try and account for the unknown location is to assign each signal a random location. Since each particle has equal probability of passing over any location, a random number was generated from a uniform distribution between -5 and 5 (the sensor spacing is 10 cm), and assigned to each signal response from the flume data. Using the normalized relations from section 4.2.1, a correction factor of 1+(1- A_{Norm}) or 1+(1- I_{Norm}) was applied to each signal response, where A_{Norm} and I_{Norm} were calculated using the absolute value of the random location. Assuming the random location is correct, the correction factor adjusts the signal response to what it would have been had the particle passed over the center of the sensor.

The empirical models for amplitude and integral were used to estimate the particle size for the adjusted data. The results from the integral model are plotted in Figure 4.23. There is still a large amount of variability in the data, but this time the data are spread more evenly about the 1:1 line.

The models do not predict an individual particle very accurately, but may still be useful at the event scale. Estimated values from the flume experiments were summed to produce an estimate of the total transported volume and mass. Table 4.3 compares the known total values with results from the models. The model with no location adjustment significantly underestimates. There is a range of estimates from the second model due to the random location component, but by summing over ~1800 stones, the estimated total volume from this model are in the correct range.

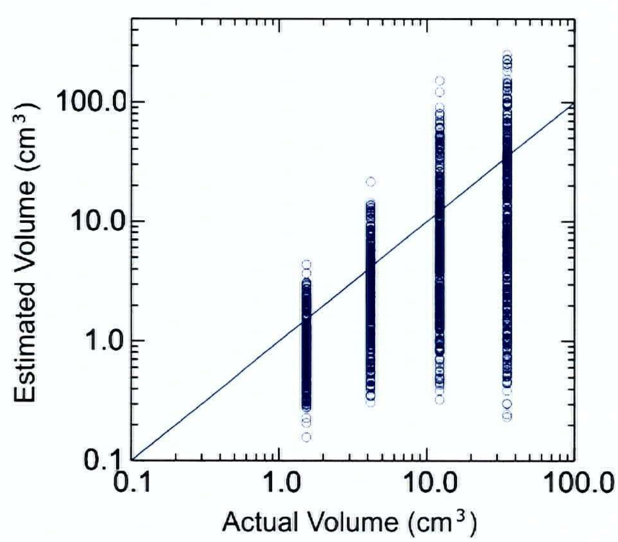

Figure 4.23. Estimated particle volumes from signal integral model with random location adjustment.

Table 4.3. Estimated total transport volume and mass from flume experiments

	Actual Amount	Estimated amount with no location adjustment	Estimated amount with random location
Volume (cm^3)	25500	8100	15000-27000
Mass (kg)	67.6	21.5	40-70

4.4 Particle Susceptibility:

To investigate the range of susceptibilities that could be expected in the field, the susceptibility of 150 stones from East Creek were measured. Fifty stones were taken from each of the 22, 32 and 45 mm size classes. To measure the susceptibility, samples needed to fit into a plastic container with a maximum volume of 10 cm^3, so only a small sample broken off of each stone was measured. The results range from 0.7 – 9500 SI units, with a geometric mean of ~200. A histogram of the results is shown in Figure 4.24.

The histogram is divided into two categories, no response and response. Before the susceptibilities were measured, each of the stones was passed by the sensors on the rotating platter apparatus. Of the 150 stones, 103 of them recorded a response, while 46 passed by undetected. There is some overlap in susceptibilities between the two categories, but in general the threshold susceptibility for detection is around 100. There were 8 stones with a susceptibility >100 that recorded a response, and 7 stones with a susceptibility <100 that failed to record a response.

The stone with the lowest measured susceptibility that recorded a response had a susceptibility of 12.3, while the stone with the largest susceptibility that failed to record a response had a susceptibility of 2970, suggesting that for some stones, the small samples used to measure their susceptibility were not representative of the rest of the stone.

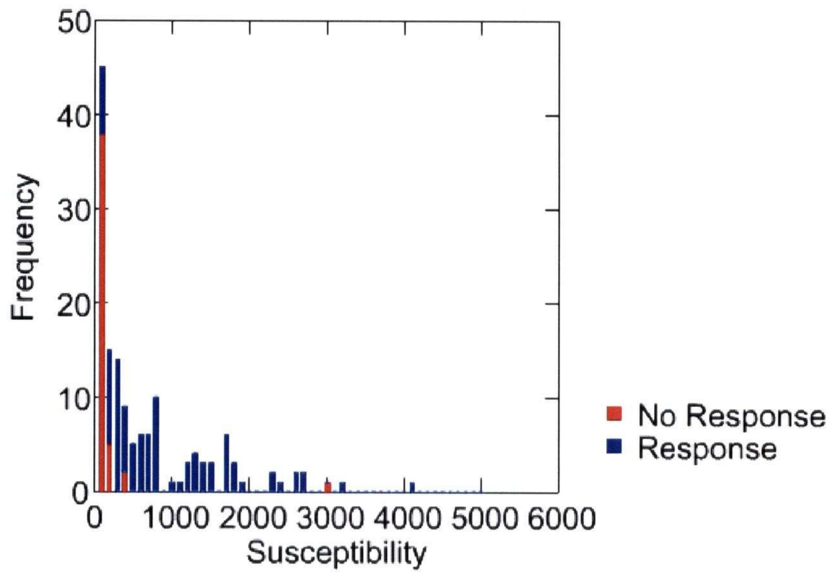

Figure 4.24. Histogram of particle susceptibilities measured from 150 stones from East Creek. The red bars indicate stones that past by the sensors with no response; the blue bars produced a response.

Using only stones with susceptibility greater than a threshold of 100, a normal distribution was fitted to the logarithm of the susceptibility data (Figure 4.25). The choice of the threshold was somewhat arbitrary, but because of the skew in the distribution, changing the threshold slightly will not have much effect. The distribution has a mean of 2.817 and a standard deviation of 0.451.

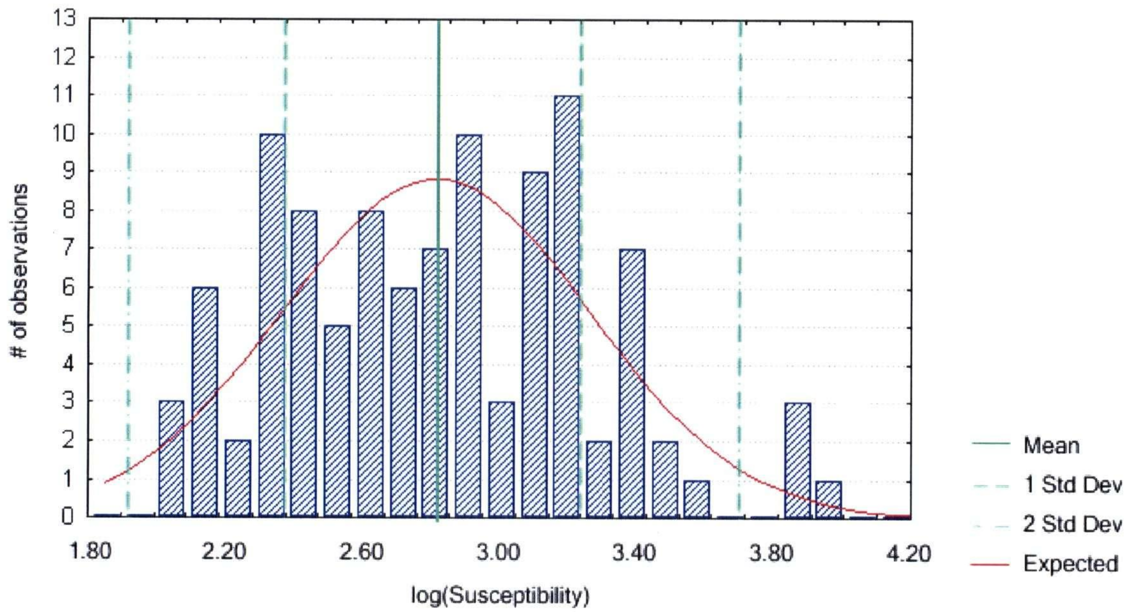

Figure 4.25. Normal distribution of the log of particle susceptibility measured from 150 East Creek stones.

When converted to arithmetic units, the geometric mean of the distribution is ~660. The range within ±1 standard deviation of the mean is 230-1860; 68% of the stones will fall within this range. Another ~13.5% of the stones will fall between 80-230 (i.e. between -1 and -2 standard deviations). These values of susceptibility are generally much lower than those of the artificial stones used to build the empirical relations. To test the ability of the relations to extrapolate back to these lower susceptibility values, volumes were estimated from the data for the East Creek rocks on the rotating platter. Figure 4.26 shows estimated versus actual volume results from using the signal integral relation. The data are divided into groups of susceptibility <1000 and >1000. The data points for the >1000 group fall relatively close to the 1:1 line; these data have susceptibilities similar to those used to calibrate the model. On the other hand, the data points from the <1000 group are significantly underestimated. This suggests that the model does not do a good job of extrapolating to smaller susceptibilities.

A second empirical model was tested using log(S) in equation 10 instead of S. This model also did a poor job of estimating at low susceptibilities. More data are required with stones of low susceptibility to investigate this relation further.

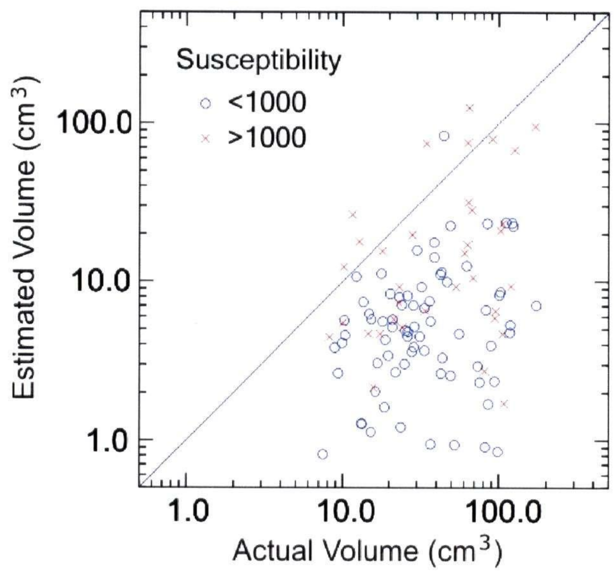

Figure 4.26. Estimated volumes of East Creek stones from the signal integral model. Susceptibilities >1000 are closer to the 1:1 line as they are in the range of susceptibilities used to develop the model.

4.5 Particle Velocity:

In order to use the signal amplitude or signal width models, the particle velocity must be known. This parameter is not generally known in the field. Other methods of bed load detection use estimates of particle velocity from theoretical calculations based on hydraulic parameters. Spieker and Ergenzinger (1988) suggested that the magnetic system could be used to measure particle velocities if two rows of sensors were used. The velocity could be determined from the time lag in signal response between the two rows.

One of the goals of the flume experiments was to test this idea. Two rows of sensors were used, spaced 22 cm apart. The signal responses from corresponding sensors were matched up, and where possible, particle velocities were calculated. For some of the signals, there was no corresponding match, because the particle was not detected over one of the rows. Particle velocities were obtained for 67% of the ~1800 signals.

As a check, particle velocities were also measured with a video camera mounted above the flume. Using a VCR with individual frame advance, the distance that a particle traveled over 8 frames was measured and translated into a velocity. Video measured velocities were matched up with the 2-row measured velocities, and are plotted in Figure 4.27. Within the error of the two systems, there is good agreement; the data fall evenly around the 1:1 line.

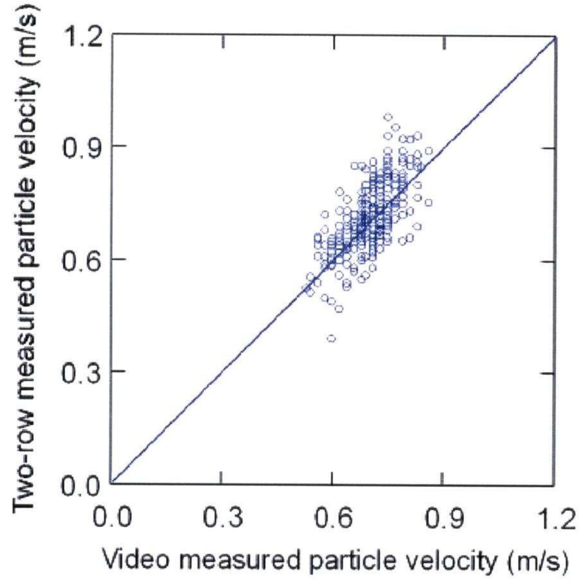

Figure 4.27. Comparison of particle velocities measured with the two rows of sensors, and the video recording.

4.6 Multiple Stone and Sand Experiments:

In both the rotating platter and flume experiments, individual particles were passed by the sensors one by one. At high transport rates, however, it is possible that multiple stones would pass by the sensor simultaneously, or in rapid succession. Experiments were carried out with multiple stones to investigate how the sensor would respond. Figure 4.28 shows the sensor response to 2 particles passing in rapid succession. The diagram is divided into four; in each section the same two particles pass by, but the spacing between the particles decreases from left to right. As the particles get closer together, the signals from the individual stones become superimposed on one another. The signals are additive, so that if the shape and location of one signal were known, it could be subtracted to leave the other signal behind. This is simple to do in the controlled lab setting, but with data collected in the field, this becomes a complex signal processing problem.

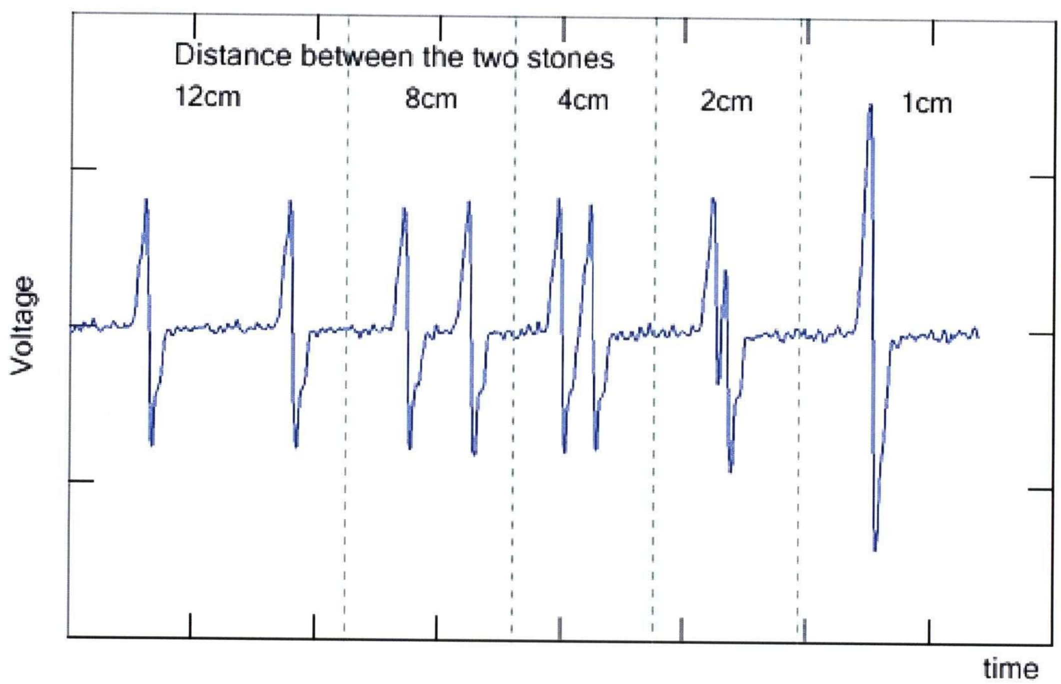

Figure 4.28. Superimposition of signals as the distance between particles decreases.

An experiment was also designed to investigate the sensor response to a mass of sand passing over. This experiment used the ramp apparatus and a sediment sample of material <8 mm taken from East Creek. A layer of sediment spanning the whole width of the sensor was passed in slurry over the sensor. Approximately 10 kilograms of sand were passed over the sensor in this manner with no visible response from the sensors. These results suggest that in the field over-passing sands will not be recorded, only the coarse fraction will, and that the fine materials will not increase the noise in the data. These results are in contradiction with results presented by Tunnicliffe et al. (2002) who presented observations of “streets” of sediment comprised of sands and gravels passing by the sensors. More experiments are required, looking at the effects of fine materials with a range of lithology to better clarify the ability of the system to detect fine materials.

Chapter 5: Discussion

5.1 Empirical Models:

The rotating platter experiments successfully showed that for the simplified case of a stone with known susceptibility passing directly over the center of the sensor, the magnitude of the signal response can be related to particle size. Of the three models developed, the width model is the poorest. Even in this simplest of cases, estimated particle size varied over 3-4 size classes, which is unfortunate, because the width is independent of susceptibility, eliminating an unknown variable from the analysis.

The model results look very similar for the amplitude and integral models, but the integral model is better, being independent of particle velocity, and having lower error. Independence from velocity is significant, because with the integral model, only one row of sensors would be required to monitor sediment transport, cutting in half the number of sensors required at a given cross-section. Also, matching up the peaks from the adjacent sensor rows to calculate particle velocities is a time consuming task that is difficult to automate.

Unfortunately, the simplified case will never be met in the field. Due to the way the signal response varies across the sensor face, and the large range of susceptibilities found in the field, the current system cannot be used to reliably estimate particle size from an individual signal.

The variation across the sensor face is due to a combination of the strength of the magnetic field from the doughnut-shaped magnet, and the distance of the stone from the center of the coil. The effect due to distance from the coil is inherent to the physics of the sensor, but the effect due to the strength of the magnetic field can be manipulated by changing the strength and/or type of magnet used, which will be discussed further in Section 5.3.

The range in susceptibility is another factor that is inevitable in the field. It may be possible to make some assumptions to simplify the problem, but unfortunately this cannot be tested further with data from the current sets of experiments. The susceptibilities of the artificial stones were chosen in order to get a strong response, well above the noise range of the sensor, so that clear relationships could be developed. However, because the empirical models do not extrapolate well to the lower susceptibilities found in the field, the analysis that can be done with these data is somewhat limited. Further experiments are required at the lower susceptibilities to better describe the relationship between susceptibility and signal response.

The current system may not be reliable for estimating the size of each individual particle, however, the system is still useful for studying patterns of spatial and temporal variability of the intensity of movement, and results from the flume experiments show that at event time scales, where the variability can average out, the system can be used to estimate transport volumes. These estimates could be further improved through field calibration against volumes collected in a sediment trap.

5.2 Problems with the Current Sensor Design:

Over the course of the experiments, some inherent weaknesses of the sensor design were observed. As described in Section 2.1, and shown in Figure 2.3C, the expected signal is a simple clean curve with a peak followed by a valley. While the majority of signals recorded resembled this ideal shape, some irregular signals were also recorded.

Sometimes, instead of the ideal curve, a double-peaked response was recorded. This effect was especially noticeable with small stones at low particle velocities. The double peak made measurement of the signal parameters more difficult, causing the peak detection sequence to pick up extra peaks. Therefore, additional processing was required to identify the double peaks and clean up the data. The double peaks especially hindered the signal width measurements, which were determined from the time difference between the peak and the valley. If the peak or valley was poorly defined, this introduced variability into the width measurement, which is already very sensitive to changes in particle size.

In the lab experiments it was known that only one particle passed by the sensor at once. In the field case, however, this will not be known and double peaked signals may be mistaken for multiple stones passing in rapid succession. For the current experiments, when two peaks were identified very close together, the lower of the peaks was discarded.

The double peak effect is most likely caused by the magnetic field created by the doughnut shaped magnet. As shown in Figure 2.4, near the sensor face, the strength of the magnetic field is highly variable, and even goes negative in the doughnut hole. The effect decreases quickly with height above the sensor, so that by 2.5 cm above the sensor the field is defined by a smooth curve, but the smallest detectable particles pass directly through this highly variable zone.

Two other effects were observed that are also likely attributable to the field of the doughnut-shaped magnet. First, in Figure 4.18, which shows how signal width changes across the sensor face, there is a distinct dip in width near the center of the sensor. The region in which this observed directly corresponds with the diameter of the doughnut hole. Secondly, in Figures 4.19 and 4.20, which show the relationship between the distance between the center of the stone and the center of the sensor coil with signal amplitude and integral respectively, the data closest to the sensor deviate from the power relation observed at greater distances. This deviation is again likely because the stones near the sensor face are moving through such a highly variable field.

Another weakness of the current sensor design is that many stones pass between sensors undetected. Because each sensor is isolated from its neighbor by a steel casing, the area at the edge and in between the sensors has a very weak field. It was thought that large stones passing between sensors would induce simultaneous response in multiple sensors; however, stones as large as 45 mm were capable of passing between sensors undetected. On the other hand, stones with high susceptibility often induced an inverted response in the adjacent sensor (i.e. a valley first, followed by a peak). This type of response was recorded for particles as small as 22 mm. These responses were large enough to be picked up by the peak detector, which was cause for additional data processing. Individual signals were identified as peak-valley pairs; valley-peak pairs were discarded.

A third weakness of the sensor is that a large range of particle sizes is described by a fairly small range of response. For example, from Figure 4.10, at a susceptibility of 1600, all 8 size classes are defined over the range 2 – 200x10^{-6} V*s. The range becomes even more constricted at smaller susceptibilities. The variability in a given integral measurement is on the order of 2x10^{-6} V*s, so that as the range becomes smaller, the ability to resolve different particle sizes decreases.

The range of response could be increased if the sensor coil responded more strongly to the passing particles. The current sensor coil is made of 40 gauge magnet wire with ~3000 winds wrapped around a ferrite core; it has an inductance of 108 mH. The inductance could be increased by increasing the number of winds on the coil, increasing the cross-sectional area of the coil, or by using a core with higher magnetic permeability. Another alternative is to increase the strength of the magnet used.

5.3 Suggestions for a New Sensor Design:

Recognizing the weaknesses of the current design, ideas were developed to improve the sensor. The first suggestion is to use a solid block magnet instead of a doughnut shaped magnet. This would produce a more uniform field for the particles to pass through.

Instead of shielding each magnet separately, block magnets could be connected end to end, in essence producing one large magnet that could span the channel width. This large magnet could then be set in a steel yoke which would act to strengthen the field near the magnet.

With a block magnet, the coils would sit on top of the magnet instead of being inset in the magnet like the current design. This design would cause the magnet to be further away from the sensor face, thereby decreasing the field strength. However, it may be a worthwhile tradeoff in order to produce a more uniform field; it may also be possible to increase the strength of the magnet to make up for this loss.

In order to keep the magnet as close to the sensor face as possible, the coils would have to be designed as thin as possible. It would be possible to reproduce the current coil design with a thickness of 6 mm. Taking into account the observations from Section 5.2 it would also be worthwhile to test ways of increasing the inductance of the coil.

By using one large magnet, and placing the coils on top of the magnet, the spacing of the coils could be decreased, further increasing the spatial resolution of the system. The limit on coil spacing would be the coil diameter, and the number of channels available from the recording system.

More importantly, because there would be no shielding between coils, a particle would pass through the same uniform field whether it passed over the center of the coil, or some distance to the side of the coil. In this case, sensor response with location across the coil array would only depend on the distance between the center of the stone and the center of the coil. As well, because of the uniform field, particles would be less likely to pass the sensor array undetected. It would be more likely for one stone to induce a response in multiple coils. By looking at the strength of response from adjacent coils, it may be possible to determine the location the stone. Additionally it may be possible to estimate the size of the stone from the number of coils that respond to its passing.

Chapter 6: Conclusions

Results from this research have identified some major problems that do not allow the BMD system to be a reliable means of measuring sediment transport. A decent estimate of particle size can be made for a particle of known susceptibility, passing over the center of the sensor; however, the variability in response across the sensor face, and the wide range of particle susceptibilities found in natural stones produce too much scatter to gain meaningful estimates of particle size. At best, the current BMD system can provide a semi-quantitative picture of the spatial and temporal variability in bed load transport.

The large range in particle susceptibility is a natural phenomenon that will continue to hamper magnetic methods. On the other hand, the variation across the sensor face is due to the current sensor design. Some ideas have been discussed that may improve the sensor design; however, at this point they are speculative and untested – a potential avenue for future research.

REFERENCES:

Andrews, E.D., 1983. Entrainment of gravel from naturally sorted riverbed material, *Geological Society of America Bulletin*, 94, 1225-1231.

Andrews, E.D., 1994. Marginal bed load transport in a gravel bed stream, Sagehen Creek, California. *Water Resources Research* 30(7): 2241-2250.

Ashmore, P.E. and Church, M.A., 1998. 'Sediment transport and river morphology: a paradigm for study." *In*: Gravel Bed Rivers in the Environment. P. Klingeman, P. Komar, W. Bradley (Eds). John Wileey & Sons, Chichester. 115-148.

Ashworth, P.J., and Ferguson, R. I. 1989. Size-selective entrainment of bed load in gravel bed streams. *Water Resources Research*, 25, 627-634.

Billi, P. and Tacconi, P., 1987. Bed load transport processes monitored at Virginio Creek measuring station, Italy, *In*: International Geomorphology Part I, V.Gardiner (Ed.) John Wiley and Sons, Chichester, 549-559.

Brayshaw, A.C., 1985. Bed microtopography and entrainment thresholds in gravel-bed rivers. *Geological Society of America Bulletin,* 96: 218-223.

Bridge, J.S. and Dominic, D.F., 1984. Bed load grain velocities and sediment transport rates. *Water Resources Research*, 20(4), 476-490.

Bunte, Kristin. 1996. Analyses of the temporal variation of coarse bed load transport and its grain size distribution (Squaw Creek, Montana, USA). Gen. Tech. Rep. RM-GTR-288. Fort Collins, CO: U.S. Department of Agriculture, Forest Service, Rocky Mountain Forest and Range Experiment Station. 124p.

Church M, and Hassan, M.A., 2002. Mobility of bed material in Harris Creek. *Water Resources Research*, 38(11) 1237-1248.

Church, M., Hassan, M.A. and Wolcott, J.F. 1998. Stabilizing self-organized structures in gravel-bed stream channels: field and experimental observations. *Water Resources Research*, 43(11), 3164-3179.

Custer, S.G., 1991. A review of natural gravel transport detection experiments at Squaw Creek, Montana, 1981-1991. Unpublished Manuscript. Dept. of Earth Sciences, Montana State University, Bozeman, MT.

Downing, J., Farley, P.J., Bunte, K., Swingle, K., Ryan, S.E. & Dixon, M. 2003. Acoustic gravel-transport sensor: description and field tests in Little Granite Creek, Wyoming, Erosion and Sediment Transport Measurement in Rivers: Technological and Methodological Advances (Proceedings of the Oslo Workshop, June 2002). IAHS Publ. 283, p. 193–200

Ergenzinger, P. and Custer, S.G. 1982. First experiences measuring coarse material bed load transport with a magnetic device. *In*: Mechanics of Sediment Transport. B.M. Sumer and A Muller (Eds.), Proceedings of Euromech 156, 223-227.

Gomez, B and Church, M. 1989. An assesment of bed load sediment transport formulae for gravel-bed rivers. *Water Resources Research* 25: 1161-1186.

Ham, D.G., and Church, M. 2000. Bed-material transport estimated from channel morphodynamics: Chilliwack river, British Columbia. *Earth Surface Processes and Landforms* 25, 1123-1142.

Haschenburger, J.K. and M. Church. 1998. Bed material transport estimated from the virtual velocity of sediment. *Earth Surface Processes and Landforms* 23: 791-808.

Hassan, M.A., and Ergenzinger, P. 2003. Tracers in fluvial geomorphology, *In:* Tools in Fluvial Morphology, G.M. Kondolf and H. Piegay (eds.), John Wiley, pp. 397-423

Hassan, M.A. and Church, M. 2001. Sensitivity of bed load transport in Harris Creek: Seasonal and spatial variation over a cobble-gravel bar. *Water Resources Research* 37(3) 813-825.

Hassan, M.A., Schick, A.P. and Laronne, J.B. 1984. The recovery of flood dispersed coarse sediment particle, a three dimensional magnetic tracing method. *In*: Channel Processes – Water, Sediment and Catchment Controls, A.P. Schick (Ed.), Catena supplement 5, 153-162.

Hayward, J.A. and Sutherland, A.J. 1974. The Torlesse Stream vortex-tube sediment trap. *Journal of Hydrology* (New Zealand) 13: 41-53

Helley, E.J., and Smith, W. 1971. The development and calibration of a pressure difference bed load sampler. U.S. Geological Survey, Open File Report, 18 pp.

Hicks, D.M. and Gomez, B. 2003. Sediment Transport. *In*: Tools in Fluvial Geomorphology, G.M. Kondolf ad H. Piegay (Eds.), Wiley and Sons, Chichester, UK. 425-461.

Hubbell, D.W., 1987. Bed load sampling and analysis. *In*: Sediment Transport in Gravel-Bed Rivers. C.R. Thorne, J.C. Bathurst and R.D. Hey (Eds.), John Wiley, Chichester, p. 89-118.

Jackson, W.L., and Beschta, R.L. 1982. A model of two-phase bed load transport in an Oregon Coast Range stream. *Earth Surface Processes and Landforms*, 7, 517-527.

Langbein, W.B. and Leopold, L.B., 1968. River Channel Bars and Dunes: Theory of Kinematic Waves, US Geological Survey Professional Paper, 442L.

Leopold, L.B. and Emmett, W.W., 1976. Bed load measurements, East Fork River, Wyoming, *Proceedings of the National Academy of Sciences of the United States of America,* 73(4) 1000-1004.

Leopold, L.B. and Emmett, W.W., 1977. 1976 Bed load measurements, East Fork River, Wyoming, *Proceedings of the National Academy of Sciences of the United States of America,* 74(7) 2644-2648.

Milhous, R.T. 1973. Sediment transport in a gravel-bottomed stream. PhD thesis, Oregon State University, Corvallis, Oregon. 232pp.

Montgomery, D.R. and Buffington, J.M. 1997. Channel reach morphology in mountain drainage basins. Geological Society of American, Bull., 109, 596-611.

O'Leary, S.J. and Beschta, R.L. 1981.Bed load transport in an Oregon Coast Range stream, *Water Resources Bulletin*, 17(5) 886-894.

Parker, G. and Klingeman, P.C. 1982. On why gravel bed streams are paved, *Water Resources Research*, 18, 1409-1423.

Parker, G., Klingeman, P.C. and McLean, D.G. 1982. Bed load and size distribution in paved gravel-bed streams. Journal of the Hydraulics Division, American Society of Civil Engineers 108: 544-571.

Poirier, R. W. 2003. The effects of sockeye spawning on streambed morphology. MSc thesis. University of Northern British Columbia, Prince Geogre, BC.

Powell, D.M. and Ashworth, P.J. 1995. Spatial pattern of flow competence and bed load transport in a divided gravel bed river. *Water Resources Research* 31(3): 741-752.

Reid, I and Frostick, L.E., 1987. Toward a better understanding of bed load transport. *In*: Recent developments in fluvial sedimentology, contributions from the third International fluvial sedimentology conference. Ethridge, F., Flores, R., and Harvey, M. (eds.) Society of Economic Paleontologists and Minerologists, Oklahoma. 13-19.

Reid, I. Layman, J.T., and Frostick, L.E. 1980. The continuous measurement of bed load discharge. *Journal of Hydraulic Research*, 18, 243-249.

Reid, I., A.C. Brayshaw, and L.E. Frostick. 1984. An electromagnetic device for automatic detection of bed load motion and its field applications. *Sedimentology*, 31, 269-276.

Reid, I., Frostick, L.E., and Layman, J.L. 1985. The incidence and nature of bed load transport during flood flows in coarse-grained alluvial channels. *Earth Surface Processes and Landforms*, 10, 33-44.

Rickenmann, D., 1994. Bedload transport and discharge in the Erlenbach Stream. *In:* Dynamics and Geomorphology of Mountain Rivers. P. Ergenzinger & K.H. Schmidt (eds). Lecture Notes in Earth Sciences, 52, 53-66.

Ryan, S.E. and Troendle, C.A. 1997. Measuring Bed load in Coarse-Grained Mountain Channels Procedures, Problems, and Recommendations. *In:* Water Resources Education, Training, and Practice. Opportunities for the Next Century, American Water Resources Association, Keystone, Colorado, pp. 949-958.

Shields, A., 1936. Andwendung der Aehnlichkeitsmechanik und der Turbulenzforschung auf die Geschiebebewegung. (Application of the Theory of Similarity and Turbulence Research to the Bed load Movement: translated by Q.M. Saleh), Mitteilungen der Preussischen Versuchsanstalt fur Wasserbau und Schiffbau, 26, Berlin.

Spieker, R. and Ergenzinger, P. 1987. New developments in measuring bed load by the magnetic tracer technique. *In*: Erosion, Transport and Deposition Processes. Proceedings of the Jerusalem Workshop, March-April 1987. IAHS Publ. No. 189. 169-178

Tacconi, P. and Billi, P. 1987. Bed load transport measurements by the vortex-tube trap on Virginio Creek, Italy, *In*: Sediment Transport in Gravel-Bed Rivers, C.R. Thorne, J.C. Bathurst and R.D. Hey (Eds.). John Wiley and Sons, Chichester, 583-616.

Thorne, P.D., Williams, J.J. and Heathershaw, A.D. 1989. *In situ* acoustic measurements of marine gravel threshold and transport.' *Sedimentology*. 36. 61-74.

Tunnicliffe, J., Gottesfeld, A.S., and Mohamed, M. 2000. High-resolution measurement of bed load transport, *Hydrological Processes,* 14, 2631-2643.

Tunnicliffe, J. 2000. The UNBC bed load movement detector: calibration, initial results and analysis. MSc thesis, University of Northern British Columbia, Prince George, BC. pp120.

Wilcock, P.R., and McArdell, B.W. 1993. Surface-based fractional transport rates: mobilization thresholds and partial transport of a sand-gravel sediment. *Water Resources Research*, 29, 1297-1312.